Modelling & Development of Novel Sustainable Thermo-fluids to Maximise the Efficiency of Solar Thermal Applications

Mian Hammad Nazir [1]*, Syed Zohaib Javaid Zaidi [2], Muhammad Majid Hussain [3], Zulfiqar Ahmed Khan [4]

[1] Department of Informatics and Electronics Engineering. University of South Wales; hammad.nazir@southwales.ac.uk;
[2] Department of Chemical Engineering, University of Punjab, Pakistan, zaidi.zohaib94@gmail.com
[3] School of Engineering and Physical Sciences, Heriot Watt University, muhammad.hussain@hw.ac.uk
[4] NanoCorr, Energy & Modelling (NCEM) Research Group, Department of Design, Engineering and Computing, Bournemouth University; zkhan@bournemouth.ac.uk

* Correspondence: hammad.nazir@southwales.ac.uk

Abstract: This research introduces an innovative numerical optimisation framework to improve the thermal efficiency of heat transfer fluids (HTFs) used in solar thermal applications, while also minimising energy consumption required for pumping. The model evaluates the performance of various HTFs and aids in selecting the most suitable fluid based on its properties. Unlike previous approaches, the novelty of this model lies in the combined assessment of corrosion behavior and heat transfer properties of fluids, recognising that system performance depends on both. By optimising key parameters such as thermophysical properties, corrosion effects, Reynolds number, and channel dimensions, the model provides a governing principle for enhancing concentrated solar power systems. Effective optimisation significantly reduces pumping energy and improves fluid efficiency. To validate the model, selected HTFs were simulated, demonstrating its accuracy and applicability for various fluid types.

Keywords: Thermo-fluids; Mathematical modelling; Heat transfer fluids; Optimisation.

1. Introduction

Heat transfer fluids, also known as thermo-fluids or HTFs, serve essential roles in solar thermal applications. They are instrumental in conveying heat within solar collectors and transferring it to heat storage tanks in solar water heating systems. Additionally, these fluids facilitate the generation of electricity by engaging in heat exchange within the power cycle, as illustrated in Fig. 1. Given the multifaceted applications of HTFs in solar thermal systems, the selection of the appropriate fluid significantly impacts the overall performance of such systems [1]. When choosing a HTF, it is crucial to take into account the following properties:

1. Coefficient of thermal expansion: refers to the fractional alteration in length (or, occasionally, volume, if specified) of a material for each unit change in temperature.
2. Viscosity: signifies a liquid's resistance to sheer forces, which, in turn, affects its flow characteristics.
3. Thermal capacity: represents a material's ability to retain and store heat.
4. Freezing point: indicates the temperature at which a liquid transitions into a solid state.
5. Boiling point: signifies the temperature at which a liquid undergoes a phase change into a gaseous state.
6. Flash point: indicates the lowest temperature at which the vapour above a liquid can be ignited in air.

Citation: To be added by editorial staff during production.

Academic Editor: Firstname Lastname

Received: date
Revised: date
Accepted: date
Published: date

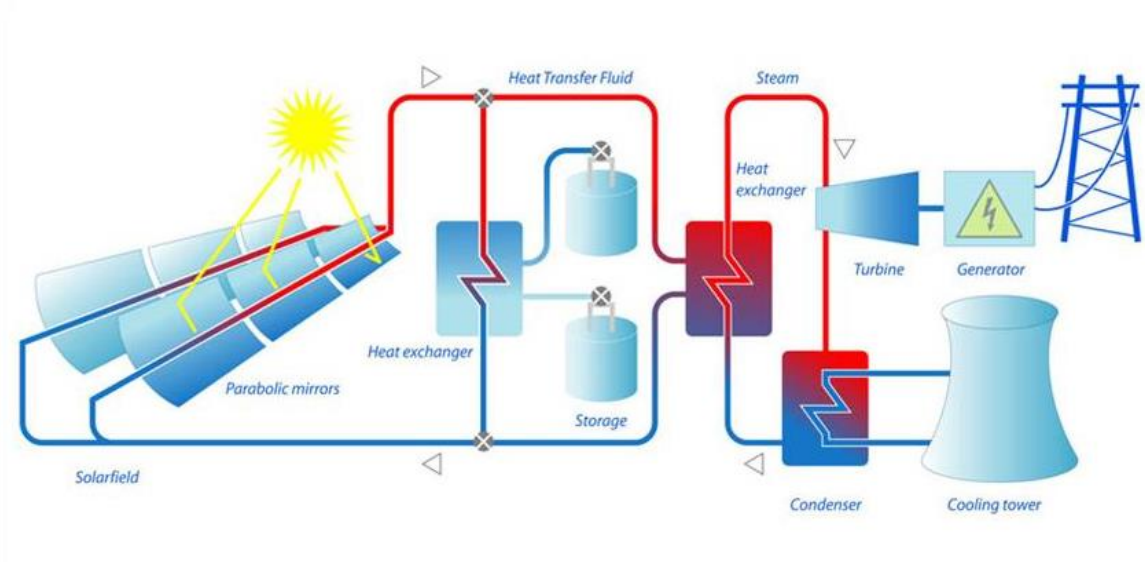

Figure 1. Heat transfer fluids are used to produce electricity through heat exchange with the power cycle.

For example, normal concentrating solar power applications require the HTFs to possess low freezing points (close to room temperature) to escape freezing during night times, high operating temperatures (> 350°C) for increasing the efficiency of the power cycle, and low vapour pressures at high temperatures for reducing the costs of installation. In heat transfer applications, the HTFs should possess high thermal capacity, high thermal conductivity and low viscosity. In addition, HTFs should be non-corrosive, environmental friendly, safe, and cost-effective [2].

In the past few years, a lot of research has been conducted in the thermophysical and corrosive properties of fluids used in solar thermal applications [3]. There are many types of fluids available commercially but two of the most famous fluids in terms of research development are mixtures (for example multi-component salts) and composite fluids (for example suspended micro-sized solid particles in liquids, commonly known as nanofluids). Many researchers and scientists have made novel developments in the area of mixtures and composite fluids which have significantly increased the performance of solar thermal applications [4-6].

The vital roles of HTFs in solar thermal applications necessitate a careful consideration of their properties for optimal system performance. While various HTFs are commercially available, research has predominantly focused on mixtures and composite fluids, which show promise in enhancing system efficiency. However, existing HTFs often fall short of meeting all performance criteria, highlighting the need for sustainable alternatives. This paper aims to analyse the existing HTFs and to develop a model which can both assist in selecting the best existing HTF for particular solar thermal applications and can also be used to develop a novel sustainable HTF by optimising the above performance properties. Strengths of this research lie in the comprehensive analysis and innovative model development, yet limitations may arise in the practical implementation of novel HTFs and the validation of the proposed model against conventional fluids.

Mathematical modeling and optimisation techniques play a critical role in advancing the efficiency and performance of heat transfer fluids (HTFs) in solar thermal applications. These methods provide the framework for analysing complex thermophysical and corrosive properties of fluids, enabling precise predictions of how these properties affect overall system performance. By using mathematical models, researchers can simulate fluid behavior under various operating conditions, making it possible to evaluate and compare different fluids without the need for extensive experimental setups. Optimisation techniques are equally important, as they allow for the fine-tuning of fluid parameters, such as viscosity, thermal capacity, and Reynolds number, to maximise efficiency while minimising costs. In particular, optimisation models can help reduce pumping energy consumption and enhance heat transfer efficiency, leading to more sustainable and cost-effective solar thermal systems.

Section 2 discusses conventional HTFs. Section 3 introduces a new optimisation model. Section 4 explores methods for optimising parameters to create sustainable fluids. Section 5 discusses the optimisation results of the new model. Section 6 validates the model by evaluating the performance of conventional fluids (water, air, oils, molten salts) using the model.

2. Conventional Heat Transfer Fluids (HTFs)

The selection of a suitable fluid for solar thermal applications is influenced by various practical factors. Table 1 provides an overview of commonly used HTFs in solar thermal power plants. A comprehensive discussion of this subject can be found in the extensive analysis conducted by reference [7].

2.1. Air and other gases

Air is a rare HTF in large-scale solar setups. Only one commercial-scale system, the Jülich solar tower in Germany (operational since 2009), uses atmospheric-pressure air as HTF [8, 9]. It heats air to around 700°C, generating steam [10]. This facility serves as a research center and prototype for future power plants in Southern Europe and North Africa, known for its cost-effectiveness and efficiency due to free and readily available atmospheric air [11]. Air's low dynamic viscosity (3×10^5 Pa s at 500°C) outperforms liquid HTFs like molten salts (200×10^5 Pa s for 'solar salt' at 500°C) and liquid metals (30×10^5 Pa s for liquid Na at 500°C) in pipeline flow [11]. Despite lower thermal conductivity than molten salts or liquid metals, air's superior flow properties benefit efficient heat transfer [5]. Europe and Israel lead air HTF research, while molten salt HTF prevails in the United States [12-16].

2.2. Water/steam

Single-fluid solar thermal systems like DSG parabolic troughs were developed in the 1980s to replace oil-based tech [17]. When the HTF isn't water/steam, heat from the receiver goes to a non-water HTF and then to water/steam. This water/steam serves as both HTF and working fluid, streamlining the system, boosting efficiency, and cutting electricity production costs [18, 19].

Ivanpah, the world's largest solar plant since Feb 2014, exemplifies this approach. Seven global commercial solar plants now use only water/steam: four in Spain (Puerto Errado 1, PS10, PS20 solar towers, Puerto Errado 2), and three in California, USA (Kimberlina, Sierra sun tower, Ivanpah). These all were built between 2007–2014 [10]. The main challenge is the limited availability of water/steam in desert regions, where these plants are mainly located due to vast land areas and intense solar radiation [20].

2.3. Thermal oils

Mineral, silicone, and synthetic oils have been tested in solar power systems as HTFs. A recent review lists global solar thermal power stations using thermal oils as HTFs [10]. These oils have nearly identical thermal conductivity (around 0.1 w/(m·K)). Their costs are $0.3/kg for mineral oil, $3/kg for synthetic oil, and $5/kg for silicone oil [21]. Radco Industries Inc. developed Xceltherm 600, a paraffinic mineral oil for solar power systems. It's used at the Saguaro Solar Power Plant in Red Rock, Arizona, USA, offering high purity and performance. These thermal oils have limited thermal stability, maxing out at 400°C [18], which hinders their use in highly efficient, high-temperature solar thermal systems. Additionally, their cost-effectiveness remains a challenge due to their relatively high cost [21].

2.4. Organics

Organic materials serve as HTFs in solar power systems. One example is Bi-phenyl/Diphenyl oxide, known as Therminol VP-1, commonly used in commercial solar plants, especially in Spanish thermal facilities. It's a eutectic blend of two stable organic compounds: Bi-phenyl ($C_{12}H_{10}$) and Diphenyl oxide ($C_{12}H_{10}O$). A recent review lists plants using this HTF [10].'Alvarado 1' in Badajoz, Spain, pioneered its use in 2009. Eight solar plants worldwide use Biphenyl/Diphenyl oxide, all in Spain. Its temperature range is 12 to 393 ^oC [10]. Therminol and Dowtherm fluids based on Biphenyl/Diphenyl oxide are commercially available. Therminol was used in a Mojave Desert solar system, and Dowtherm in Nevada Solar One in Boulder City, NV. Dowtherm's viscosity and thermal conductivity at 300 ^oC are 0.00059 Pa s and 0.01 W/(m K).

2.5. Molten-salts

Molten salts are excellent HTFs due to their exceptional thermal stability above 500 ^oC. They resemble water in viscosity and vapor pressure at high temperatures [38]. Modern solar power systems often use molten-salt-based HTFs, dating back to 1984 with systems like THEMIS tower (2.5 MWe) in France and the Molten-salt Electric Experiment (1 MWe) in the United States [22]. Molten salts are advantageous for thermal energy storage. In 1996, the United States achieved a mile-

stone with Solar Two, a 10 MWe system using molten salt for both HTF and energy storage, providing 3-hour energy storage capability. Solar Two's three-year operation was crucial for advancing molten-salt power tower technology commercialisation [22].

As indicated in Table 1, a majority of the presently employed salts for HTFs are derived from nitrates/nitrites, constituting a prevalent choice among various options. While these salts possess commendable thermal properties, it is crucial to consider the thermal stability of piping and container materials when handling salts within their specified temperature range [23].

Table 1. Thermal and physical properties of commonly used HTFs [24-26].

Name	Compositions (wt.%)	Melting point (DEGREE C)	Stability limit (DEGREE C)	Viscosity (Pa s)	Thermal conductivity (W m $^{-1}$ K $^{-1}$)	Heat capacity (kJ kg $^{-1}$ K $^{-1}$)	Cost ($/kg)	Corrosion		
								Rate (μm/year unless specified)	Alloy	Temperature (DEGREE C)
Air	Air	–	–	0.00003 (at 600 DEGREE C)	0.06 (at 600 DEGREE C)	1.12 (at 600 DEGREE C)	0	7–14 g/m[b]	Fe–Al (5.8–16.2 wt%) Cr (1.9–9.7 wt%)	1100
Water/Steam	H2O	0	–	0.00133 (at 600 DEGREE	0.08 (at 600 DEGREE C)	2.42 (at 600 DEGREE C)	0	1.7–3.5	In600	300
Mineral oil	N/A	20	300	N/A	0.1	N/A	0.3	N/A		
Synthetic oil	N/A	20	350	N/A	0.1	N/A	3	N/A		
Silicone oil	N/A	20	400	N/A	0.1	N/A	5	N/A		
Xceltherm 600	Paraffinic mineral oil	NA	315	0.001085 (at 300 DEGREE C)	0.1	2.436 (at 300 DEGREE C)	N/A	N/A		
Organics										
Biphenyl/Diphenyl	N/A	12	393	0.00059 (at	0.01 (at 300 DEGREE C)	1.93 (at 300 DEGREE C)	100	N/A		

oxide				300 DEGREE C)					
Molten-salts									
Solar Salt	$NaNO_3$ (60)–KNO_3 (40)	220	600	0.00326 (at 300 DEGREE C)	0.55 (at 400 DEGREE C)	1.1 (at 600 DEGREE C)	0.5	5	A36	316
								6–15	304	570
								15.9/4	316	600/680
								60	321	600/680
								10.4/4	347	600/680
								47	Ha230	600/680
								19.8/6	In625	
								88		
								21.7/5		
								94		
Hitec	$NaNO_3$ (7)–KNO_3 (45)–$Ca(NO_3)_2$ (40)	142	535	0.00316 (at 300 DEGREE C)	0.2 (at 300 DEGREE C)	1.56 (at 300 DEGREE C)	0.93	2	321	570
Hitec XL	$NaNO_3$ (7)–KNO_3 (45)–$Ca(NO_3)_2$ (48)	120[a]	500	0.00637 (at 300 DEGREE C)	0.52 (at 300 DEGREE C)	1.45 (at 300 DEGREE C)	1.1	6–10	304; 316	570
Na–K–Li nitrates	$NaNO_3$ (28)–KNO_3 (52)–$LiNO_3$ (20)	130	600	0.03 (at 300 DEGREE C)	N/A	1.091	1.1	N/A		
LiNaK carbonates	Li_2CO_3 (32.1)–Na_2CO_3 (33.4)–K_2CO_3 (34.5)	400	800–850	0.0043 (at 800 DEGREE C)	N/A	1.4–1.5	1.2–1.3	<1000	In600	900
K–Li–Ca nitrates	KNO_3 (50–80)–$LiNO_3$ (0–25)–$Ca(NO_3)_2$ (10–45)	<80	500	0.004 (at 190 DEGREE C)	0.43 (at 300 DEGREE C)	N/A	0.6–0.8	N/A		
Na–K–Li nitrates/ nitrites	$NaNO_3$ (14.2)–KNO_3 (50.5)–$LiNO_3$ (17.5)–$NaNO_2$ (17.8)	99	430	N/A	N/A	1.66 (at 500 DEGREE C)	N/A	N/A		
Sandia Mix	$NaNO_3$ (9–18)–KNO_3 (40–52)–$LiNO_3$	<95[a]	500	0.005–0.007	0.654 (at 250 DEGREE C)[a]	1.16–1.44 (at	0.62–	N/A		

	(13–21)–$Ca(NO_3)_2$ (20–27)			(at 300 DEGREE C)		247 DEGREE C)	0.81		
Halotechnics SS-500	$NaNO_3$ (6)–KNO_3 (23)–$LiNO_3$ (8)–$CsNO_3$ (44)–$Ca(NO_3)_2$ (19)	65	500	N/A	N/A	1.22 (at 150 DEGREE C)	N/A	N/A	
Li–Na–K fluorides/carbonates	N/A	400	900	N/A	1.17 (at 400 DEGREE C)	N/A	N/A	8–12	316L	465
~~Halotechnics SS-700~~	~~N/A~~	~~257~~	~~700~~	~~0.004 (at 500 DEGREE C)~~	~~0.35–0.4~~	0.79 (at 300 DEGREE C)		~~165~~ 276	~~316L~~ Ni201	~~700~~

3. Optimisation Model

3.1. Previous models

For obtaining the high efficiency of solar thermal system, the selection of HTF is extremely important, as it directly determines the thermal and thermodynamic performance of the solar collector field [27]. A literature survey shows that previously the performance of HTFs was evaluated by comparing their individual thermophysical properties [28]. However, for performance evaluation of HTFs it is important to consider all the properties at once in a collective manner rather than individually. Many models, as shown in Table 2, have been developed considering the collective thermophysical properties to evaluate the performance of HTFs.

Table 2. Previous models developed considering the collective thermophysical properties

Developer	Model	Reference
Mouromtseff	$N_{Eff} = \frac{\rho^{0.8} c_p^{0.33} k^{0.67}}{\mu^{0.47}}$	[29]
Bonilla	$N_{Eff} = \frac{\rho^2 c_p^{2.8}}{\mu^{0.2}}$	[30]
Murakami and Mikić	$N_{Eff} = \frac{\rho\, v^3}{L^3} \frac{Re^3}{D_h^4} A$	[31]
Andrej	$N_{Eff} = \frac{\rho^2 c_p^{1.6} k^{1.3}}{\mu^{1.4}}$	[32]

Mouromtseff utilised the Dittus-Boelter correlation to evaluate the combined effects of fluid properties on the convective heat transfer coefficient of internal turbulent flow represented in the form of system efficiency N_{Eff} [29]. The Dittus-Boelter correlation, which relates the Nusselt number to the Reynolds and Prandtl numbers, allowed for the assessment of heat transfer performance under turbulent conditions by accounting for key fluid properties such as thermal conductivity, viscosity, and specific heat. However, this approach primarily focused on fluid characteristics in the radial direction, while omitting considerations related to axial flow behavior or pumping power requirements.

In contrast, Bonilla proposed an alternative model for calculating system efficiency N_{Eff} by comparing the required pumping power needed to maintain a specified temperature difference between the inlet and outlet of the carrier fluid [30]. However, Bonilla's model had its own limitations, as it neglected the radial direction entirely and only considered fluid characteristics along the axial flow direction.

Subsequently, Murakami and Mikić optimised the efficiency N_{Eff} of heat sinks by minimising the pumping power and assuming the same temperature difference between the wall outlet and fluid inlet [31]. However, despite these advancements, their model still exhibited a critical limitation: it overlooked the fluid pumping power requirements, which are essential for practical applications.

Recently, Andrej modified Murakami and Mikić's model by addressing all the above effects [32]. They introduced dimensionless pumping and thermal loads and showed important relationships among the parameters to optimise heat sink designs considering the axial and radial heat flow as well as the pumping power requirement. However, Andrej ignored the corrosive, environmental friendly, safe, and cost-effective properties of HTFs [33]. Here, the methodology suggested by Andrej is employed to develop a new optimisation model for evaluating the performance of conventional solar thermal HTFs.

3.2. New optimisation model

Fig. 2 shows a schematic of a solar thermal panel with 'n' number of solar collector tubes. Each solar collector tube can be represented as a single channel of diameter D and length L. It is assumed that the heat flux is uniform throughout the length of the tube. The temperature gradient inside the solid walls of the tube is ignored, and is only considered inside the fluid.

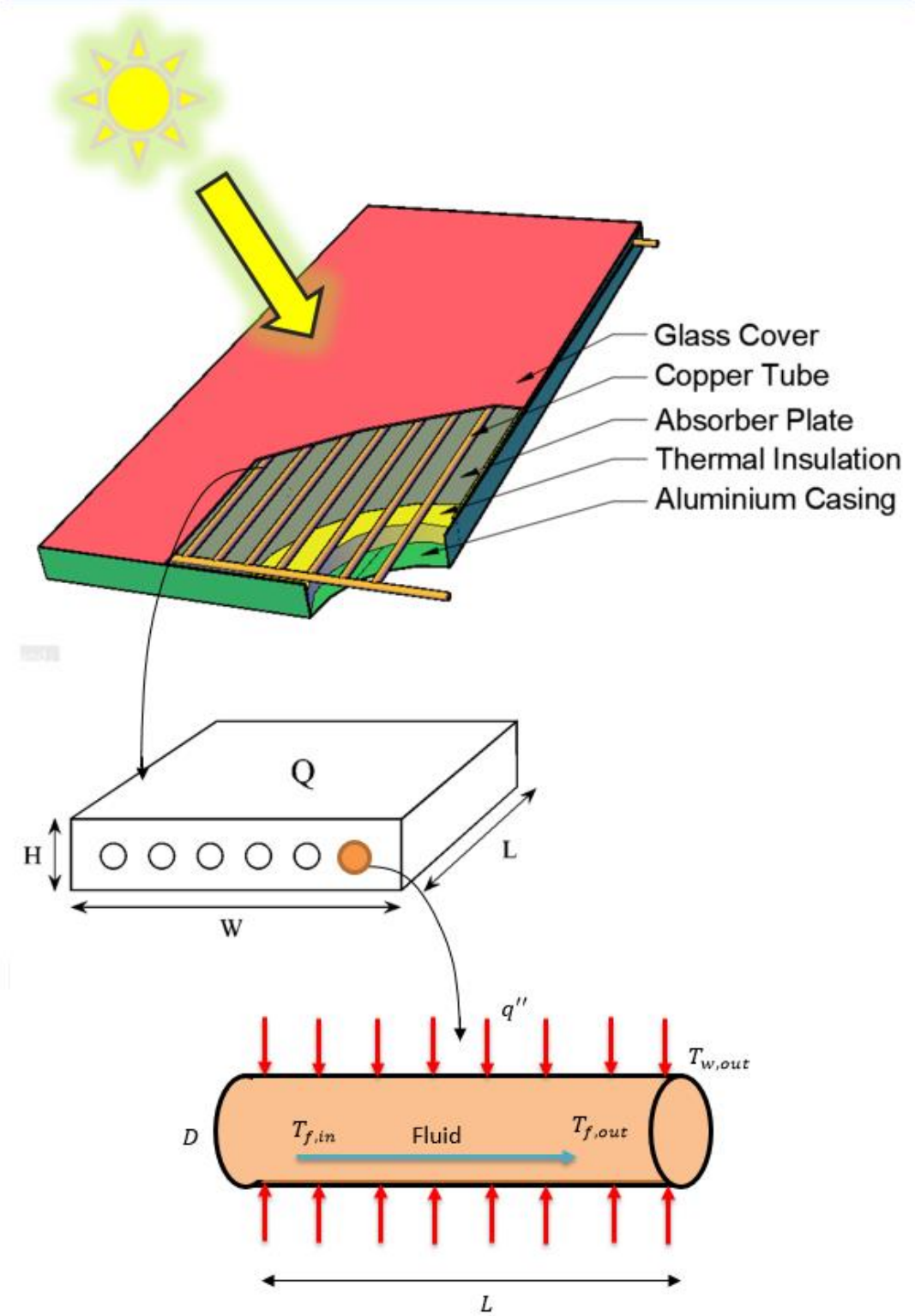

Figure 2. shows a schematic of a solar thermal panel with 'n' number of solar collector tubes. Each solar collector tube is represented as a single channel with specific dimensions (diameter D and length L). T_w,out indicates the outlet wall temperature, while $T_{f,in}$ and $T_{f,out}$ represent the inlet and outlet temperatures of the heat transfer fluid (HTF), respectively.

Following assumptions are made concerning the fluid flow in the channel:

Assumptions:
a) Constant (or uniform) heat flux input at the channel wall
b) thermally/hydrodynamically fully developed flow;
c) constant fluid properties;
d) incompressible flow;
e) steady state;
f) no gravity effect;
g) no surface roughness on the channel wall;
h) no viscous heat generation
i) heat flux q'', tube length L, and the maximum temperature difference between the tube wall and fluid inlet (ΔT) are fixed.

These assumptions collectively create a framework for simplified yet accurate modeling of fluid behavior and heat transfer in solar thermal systems. While certain assumptions may introduce minor deviations from reality, their necessity lies in reducing computational complexity while maintaining practical relevance.

3.2.1. Heat transfer induced by temperature gradient equations

With the stated assumptions (a to i), new equations have been derived. It can be seen from assumption (a) that since constant (or uniform) heat flux input at the channel wall has been assumed, therefore, the heat flux q'' at the channel wall is expressed as [34],

$$q'' = \frac{Q}{npL} \tag{1}$$

Where p represents the perimeter of a channel; L is the length of a channel; n is the total number of channels and Q is total heat dissipation from a heat source.

The heat flux q'' is used to calculate the rise in temperature of the fluid flowing through a channel of thickness h which is expressed as [35],

$$T_{f,out} - T_{f,in} = \left(T_{w,out} - T_{f,in}\right) - \left(T_{w,out} - T_{f,out}\right) = \Delta T - \frac{q''}{h} \tag{2}$$

The symbols T_w and T_f refer to the temperature at the surface of the channel wall and the average temperature of the fluid in that location, respectively. Consequently, $T_w - T_f$ signifies the temperature difference between the channel wall and the fluid at that point. ΔT represents the maximum temperature difference, which is defined as $T_{w,out} - T_{f,in}$. In the context of solar thermal collector tubes, the stability of the HTF and the properties of the selective coating impose a limitation on the value of $T_{w,out}$.

The bulk velocity of the fluid inside the tube follows the law of conservation of energy as [36],

$$q''aLp = \rho VAc_p(T_{f,out} - T_{f,in}) \tag{3}$$

where V and p represent the average bulk velocity of the fluid and the perimeter of the tube, respectively; ρ is the density of the fluid; A is the cross-sectional area of the flow channel; c_p is the specific heat capacity of the fluid at constant pressure; L is the length of the channel; a is the correction factor for the case when the heat flux is applied to a fraction of the perimeter.

The pumping power of fluid is normalised by the amount of heat transferred to the fluid per time as [37],

$$\overline{P} = \frac{\Delta PVA}{q''apL} = \frac{1}{8a}\frac{Y}{\Lambda}\frac{f\,Re^3}{\overline{D}^3} \tag{4}$$

Where f stands for the internal friction factor [27], Y is used to represent the dimensionless pumping load, while Λ and $\overline{D}$ are used to indicate a dimensionless thermal load and a dimensionless hydraulic diameter, respectively. The significance of Λ can be understood as the degree of heat removal demand: A higher value of Λ indicates a greater need for pumping work to meet a specified thermal constraint, k_f is the thermal conductivity of the fluid; ΔT_{max} is the maximum temperature difference across a certain length of the fluid channel and ΔP represents the pressure drop [37]. Where,

$$Y = \frac{\rho V^3}{k_f \Delta T_{max} L^2}$$

$$\Lambda = \frac{Q}{k_f \Delta T_{max}} . \frac{L}{S} \quad (5)$$

$$\bar{D} = \frac{D}{L}$$

$$\Delta P = \frac{f}{2} . \frac{\rho v^2}{L^2} . \frac{Re^2}{\bar{D}^3}$$

Where, ΔP is the pressure drop across a length of the fluid flow channelS is represents a characteristic cross-sectional area; $\bar{D}$ denotes a non-dimensional or normalized diameter; D represents the actual diameter of a flow channel; f is the Darcy-Weisbach friction factor, which is a dimensionless number that represents the friction losses in the fluid flow due to the viscosity of the fluid.

Substituting eq. 3 and 5 in eq. 2 gives

$$1 = \frac{\Lambda \bar{D}}{N_u} + F_N \quad (6)$$

Where Nu represents the Nusselt number; F_N is the normalised temperature rise of the fluids $(T_{f,out} - T_{f,in})/\Delta T$ given as [36]:

$$F_N = \frac{4a\Lambda}{Re.\frac{\mu c_p}{K_M}} \quad (7)$$

With the eq. 1, 2, and 3, the Reynolds number Re can be expressed using dimensionless groups as,

$$R_e = \frac{VD}{v} = \frac{\Lambda \bar{D}}{\frac{\mu c_p}{K_M}\left(\overline{A} - \frac{\Lambda \bar{D}^2}{4N_u}\right)} ; \quad \left[\overline{A} = \frac{A}{S}\right] \quad (8)$$

Where K_M in eq. 8 is the mass transfer coefficient [38]; v is the kinematic viscosity of the fluid; $\overline{A}$ is the ratio of channel area A to heat sink area S. Both $\overline{A}$ and Λ are specified in this optimisation scheme.

In the context of fully developed turbulent flow within a smooth circular channel, the provided equations for the friction factor denoted as 'f' and the Nusselt number represented as 'Nu' have been validated as precise over a broad spectrum of Reynolds numbers [39].

$$f = 0.184\ Re^{-0.2} \quad (9)$$

In general, the Nusselt number can be written as [38],

$$N_u = \frac{hL}{K_M} \quad (10)$$

3.2.2. Mass transfer driven corrosion equations

In high-temperature solar power systems, HTFs like molten salt cause corrosion in receivers and heat exchangers, impacting efficiency and system lifespan. Managing high-temperature corrosion is vital for prolonged system life, better heat transfer, and economic viability [40].

A corrosion model considers factors like fluid flow and selective oxidation in alloys when in contact with HTFs [41]. This model predicts corrosion rates and potentials by combining the reaction mechanism with computational fluid dynamics (CFD). CFD simulations assess flow patterns driven by natural convection in the channel, analysing dimensionless engineering parameters like the Nusselt number (Nu) and Grashof number (Gr_m). These parameters help estimate mass transfer coefficients and boundary layer thickness, crucial for corrosion rates. The model suggests that selective oxidation in the channel is influenced by mass transfer, and could be further aggravated in solar power systems with forced convection.

Dimensionless analysis correlates temperature-induced heat transfer and mass transfer-driven corrosion[42]. Mass transfer plays a role similar to heat transfer, but the governing equations for heat and mass transfer have distinct coefficients [43, 44].

$$\mathrm{Gr_m} = \frac{g(\rho_\infty - \rho_o)L^3}{\rho_\infty \nu^2} \quad (11)$$

$$\mathrm{Sc} = \frac{\mu}{\rho D_{salt}} \quad (12)$$

$$\mathrm{Sh} = \frac{K_M L}{D_{GB,salt}} = 0.62(\mathrm{Sc}\ \mathrm{Gr_m})^{0.25} \quad (13)$$

In the context of dimensionless analysis applied to free convection, $\mathrm{Gr_m}$ represents the relationship between the buoyancy force and the viscous force acting on the fluid during natural convection [45]. In the realm of natural convection, $\mathrm{Gr_m}$ assumes a role similar to that of Re in forced convection, where Re signifies the ratio of inertial force to viscous force experienced by the fluid. Similarly, the Sc number denotes the ratio of viscous momentum to the diffusion of species, similar to how the Pr number operates. Additionally, the Sh number stands as the ratio of mass transfer coefficients, comparable to the Nu number for heat transfer.

In the context of correlating heat transfer to mass transfer-driven corrosion, other essential dimensionless parameters include K_M in eq. 10 and eq.13 where K_M effects the N_u in heat transfer equations which further effects the normalised temperature rise of the fluids F (in eq. 7) and pumping power $\overline{P}$ (in eq. 4).

3.2.3. Corrosion model equations

To create a corrosion model, integration involved incorporating a diffusion-limited corrosion mechanism identified through electrochemical analyses and SEM/EDS investigations of the Fe-Ni-Cr alloy [46, 47]. The SEM/EDS images presented in Fig. 3 illustrate the consequences of exposing the Fe-Ni-Cr alloy to a Molten Salt Heat Transfer Fluid, specifically $MgCl_2$ - KCl, at a temperature of 850 ℃ for a duration of 100 hours. These images reveal a depletion of chromium (Cr) on the surface as well as along grain boundaries. It is worth noting that other research studies have also documented selective chromium oxidation along grain boundaries [48-51].

The corrosion model, which has been developed as part of this study, incorporates the self-diffusion of chromium (Cr) within bulk alloys, allowing it to migrate towards the surface along with grain boundaries, followed by subsequent Cr oxidation reactions. To address the lack of published data on Cr diffusion in Haynes 230 and Cr^{2+} and Cr^{3+} diffusions in $MgCl_2$-KCl, self and grain boundary diffusion coefficients for Cr in Ni plate and Fe^{3+} in $MgCl_2$-KCl were utilised [48-51], as well as Cr^{2+} and Cr^{3+} complexes in KCl-NaCl.

The Arrhenius fits and Hart equation were employed to ascertain the pre-exponential factor and activation energy associated with lattice and grain boundary diffusions [46, 52].

$$D_A = A_r \exp\left[-\frac{E}{RT}\right] \quad (14)$$

Where, D_A represents the diffusivity or the diffusion coefficient of species AAA in a medium; E is the activation energy, R is the universal gas constant; T: This is the absolute temperature, A_r is the pre-exponential factor.

The subsequent initiation reactions, as well as the reduction reaction step in the propagation process, are presumed and employed in the model [53].

Initiation reactions

Oxidation reaction: $Cr_{23}C_6 + 69Cl^- \rightarrow 23CrCl_3 + 6C + 69e^-$ (15)

Reduction reaction: $34.5MgCl_2 + 34.5H_2O + 69e^- \rightarrow 34.5H_2 + 34.5MgO + 69Cl^-$ (16)

Propagation (alloy and salts)

Oxidation reaction: $Cr + 2Cl^- \rightarrow CrCl_2 + 2e^-$ (16)

Reduction reaction: $2CrCl_3 + 2e^- \rightarrow 2CrCl_2 + 2Cl^-$ (17)

Disproportionation (Crucible)

Oxidation reaction: $2CrCl_2 + 2Cl^- \rightarrow 2CrCl_3 + 2e^-$ (18)

Reduction reaction: $Ni + CrCl_2 + 2e^- \rightarrow NiCr + 2Cl^-$ (20)

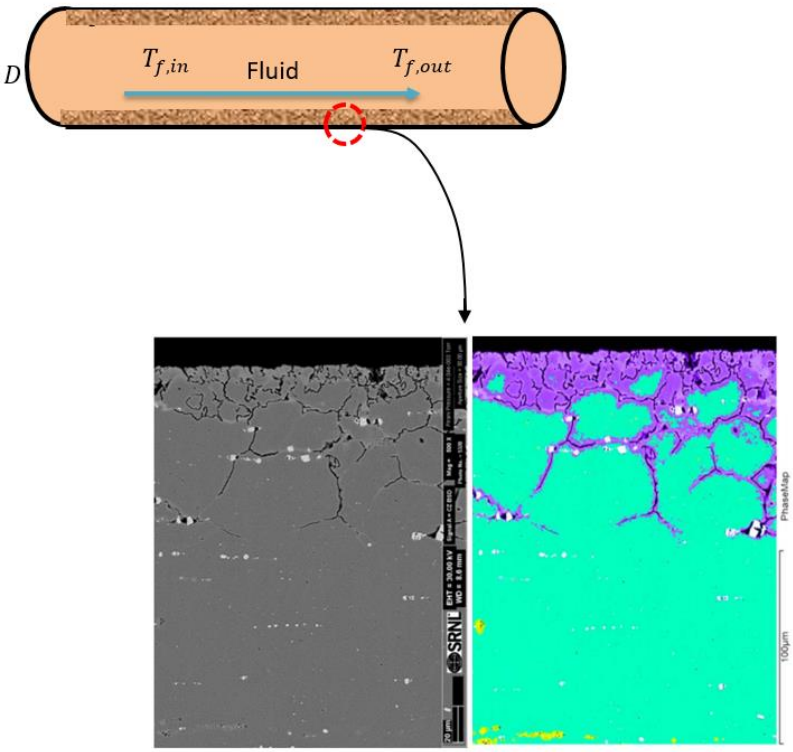

Figure 3. The top image shows a single solar collector tube represented as a single channel. The inner boundary of the channel shows the corrosion with the fluid flowing inside the channel. The lower image shows the microscopic image of high-temperature corrosion.

The Cr oxidation reaction was primarily selected (with a weight percentage of 22.08%) for our model predictions, given the lower Mn (0.52 wt%) content in the Fe-Ni-Cr alloy [54]. Additionally, it's worth noting that $Cr_{23}C_6$ represents the primary type of chromium carbides that form in Fe-Ni-Cr alloys. In cases where concentration gradients in the solution are negligible, the solute species (Ni) flux can be expressed as [55]:

$$N_i = -z_i u_i F c_i \nabla \Phi + v c_i \quad (19)$$

Where, $\mathbf{z_i}$ is the charge number of species i; $\mathbf{u_i}$ represents the mobility of species I; $\boldsymbol{\nabla\Phi}$ represents the gradient of the potential Φ; $\mathbf{v_{ci}}$ refers to an additional velocity term for species i, related to convection. Also, the current density (i) in an electrolyte solution (l) is due to the flux of charged species and can be written [56]:

$$i_l = F\sum z_i N_i \tag{20}$$

Substitution of eq. 21 into eq.22 yields

$$i_l = -\sigma_l \nabla \Phi_l \tag{21}$$

Where $\sigma_l = F^2 \sum_i z_i^2 u_i c_i$ is the conductivity of the electrolyte. The sum of the convective fluxes for the charged species in eq. 21 is also zero due to electro-neutrality. The electro-neutrality states that the electrolyte (solution) is electricity neutral due to the repairing force resulting from the separation of charge [57].

$$\sum z_i c_i = 0 \tag{22}$$

From the law of the conservation of mass and energy along with eq. 21 and eq. 22,

$$\nabla . N_i = 0 \tag{23}$$

$$\nabla . i_l = 0 \tag{24}$$

Substituting eq. 23 in eq. 26 results in the Laplace equation representing the potential [58]. Recent studies [59, 60] have demonstrated the practicality of employing the Laplace equation to simulate the distribution of steady-state current and potential in the context of corrosion under conditions of a thin electrolyte [61].

$$\nabla^2 \Phi_l = 0 \tag{25}$$

The Tafel equation is used to explain the electrochemical kinetics of the corrosion [61].

$$i_{loc,m} = \left(\frac{c}{c_{ref}}\right) i_{0.m} \exp\left(\frac{\eta}{\beta_a}\right) \tag{26}$$

$$\eta = \Phi_m - \Phi_l - E_{eq,m} \tag{27}$$

Also, the metal-salt boundary interface sets the [61]

$$i_l = \sum_m i_{loc,m} \tag{28}$$

For the cathodic species (see eq. 18), the Tafel expression corrected by the concentration term is used, which set the local current density to [61]

$$i_{loc,cathode} = -\left(\frac{c}{c_{ref}}\right) i_{o,cathode} \exp(\frac{\eta}{\beta_a}) \tag{29}$$

The transport of chromium (Cr) within the bulk alloy, across grain boundaries, and via the diffusion and convection of cathodic species (Cr^{3+}) is considered by employing eq. 25 to calculate the species flux and adhering to the principle of mass conservation [62].

$$N_i = vc_i - D\nabla c_i \tag{30}$$

$$\nabla . N_i = 0_i \tag{31}$$

On the metallic surface adjacent to the grain boundary, the anodic and cathodic species' flux is coupled to the Cr oxidation current density, assuming a boundary condition of limited current:

$$n.N = \frac{s\, i_{loc,Cr}}{nF} = -K_M(C_S - C_{bulk}) = -K_M(0 - C_{bulk}) \tag{32}$$

Where n is the normal vector, S is the surface, s is the stoichiometry number.

The local mass transfer coefficient, denoted as K_M, was determined using eqs. 10 and 13. This coefficient takes into account the fluid properties in close proximity to the sample during the calculation process. To anticipate the corrosion products of alloys in molten salts and assess the oxidation and reduction reactions potentially occurring at the alloy surface, the minimisation of Gibbs energy, as outlined in reference [63], was employed. Furthermore, thermodynamic modeling was utilised to predict the eutectic temperature of salt systems. This prediction was based on the Gibbs energies associated with the fusion of individual salts and the mixing of constituent binary systems, as detailed in reference [63]. To illustrate, the Gibbs energy of formation (ΔG^o) for the reaction aA + bB = cC was computed at various temperatures in accordance with eq. 35. Subsequently, the standard reduction potentials (E^o) at different temperatures were derived using the fundamental relationship between ΔG^o and the electrochemical potential at equilibrium, denoted as E^o (as shown in eq. 36) [62, 64].

$$\left(\frac{\Delta G_c^o}{T}\right) = \left[\frac{\Delta H_{f0}^o}{T} + \frac{\Delta G_T^o - H_0^o}{T}\right]_c - \frac{a}{c}\left(\frac{\Delta G_T^o - H_0^o}{T}\right)_A + \frac{b}{c}\left(\frac{\Delta G_T^o - H_0^o}{T}\right) \tag{33}$$

$$\Delta G^o = -nFE^o \tag{34}$$

$$E = E^o - \frac{RT}{nF}\ln\prod a_i^{\,s_i} \tag{35}$$

3.2.4. Pumping power required

Substituting eq. 5-9 into eq. 4 gives:

$$\overline{P} \propto \frac{Y\Lambda^{2.4}}{Pr^{1.6}} \; \frac{1}{F_N^{0.4}(1-F_N)^3} \tag{36}$$

As per assumption (i) the heat flux q'', tube length L and the maximum temperature difference between the tube wall and fluid inlet (ΔT) are fixed, the normalised pumping power is determined by the properties of the fluid and the Reynolds number Re (in eq. 8). To clarify the effect of fluid properties on the normalised pumping power without introducing complexity associated with the Reynolds number, the normalised temperature rise (F_N) is solved by initially solving eq. 21, 22, 23, and 34 for the mass transfer coefficient (K_M). Subsequently, by substituting this value into equation 7, the result is obtained:

$$F_N = \frac{4aQLnN}{Re.\mu\, c_p C_{bulk} k_f \Delta T_{max}\, S} \tag{37}$$

By substituting eq. 39 into eq. 38, the normalised pumping power can be described as:

$$\overline{P} \propto \left[\frac{\mu^{1.4}}{\rho^{2.0} c_p^{1.6} k^{1.8}}\right]\left[\frac{q''^{\,2.4}}{\Delta T_{max}^{3.4}}\right] \frac{1}{\left[\left(\frac{4aQLN}{Re.\,\mu\, c_p C_{bulk} k_f \Delta T_{max}\, S}\right)^{0.4}\left(1 - \frac{4aQLN}{Re.\,\mu\, c_p C_{bulk} k_f \Delta T_{max}\, S}\right)^3\right]} L^{0.4} \tag{38}$$

The performance of HTFs N_{Eff} is determined by the combination of fluid properties in the first braces and corrosive properties and Reynolds number Re in the second braces. Since the normalised pumping power needs to be minimised, the new optimisation model of solar thermal HTFs becomes:

$$N_{Eff} = \underbrace{\frac{\rho^{2.0} c_p^{1.6} k^{1.8}}{\mu^{1.4}}}_{\text{Thermophysical properties}} \underbrace{\frac{1}{\left(\frac{4aQLN}{Re.\mu\, c_p C_{bulk} k_f \Delta T_{max}\, S}\right)^{0.4}\left(1-\frac{4aQLN}{Re.\mu\, c_p C_{bulk} k_f \Delta T_{max}\, S}\right)^{3}}}_{\text{Corrosive properties}} \quad (39)$$

4. Development of a New Sustainable HTF by Using Novel Optimisation Model

This section presents an optimisation study of solar power system. Specifically, a method has been presented for determining the optimum values of the thermophysical parameters of HTF, corrosion parameters of HTF, flow rate of HTF, channel diameter, and number of channels for minimum pumping power or minimum pressure drop. For optimisation, the newly developed optimisation model in section 3 (eq. 41) has been used. The optimised parameters are represented without dimensions. The calculated outcomes in both the laminar and turbulent regimes reveal several significant connections among these parameters. Herein, a criterion for selecting the HTF for use in a solar power system is introduced.

The aim of this research is to establish an optimisation technique aimed at reducing the energy required for pumping or pressure drop in response to a solar power system. To date, several studies have been conducted concerning the optimisation of HTFs [65-67]. In all of these investigations, thermal resistance has been selected as the parameter to be minimised, while specifying the pressure drop or pumping power. In this section, the term "minimised parameter" denotes a parameter that the optimisation process seeks to minimise.

4.1. Optimisation of Thermophysical and Corrosive properties of HTF

The development of HTF is essential to the feasibility and efficiency of solar thermal power plants, as it determines the pumping power and power load of the collector field. In this chapter, the performance of HTFs was determined by a combination of thermophysical and corrosive properties rather than by each of the individual properties. In section 3, a new optimisation equation for pumping power was derived:

$$\left[\frac{\mu^{1.4}}{\rho^{2.0} c_p^{1.6} k_f^{1.8}}\right]\left[\frac{q''^{2.4}}{\Delta T_{max}^{3.4}}\right]\left[\frac{1}{\left(\frac{4aQLN}{Re.\,\mu\, c_p C_{bulk} k_f \Delta T_{max}\, S}\right)^{0.4}\left(1-\frac{4aQLN}{Re.\,\mu\, c_p C_{bulk} k_f \Delta T_{max}\, S}\right)^{3}}\right] L^{0.4} \quad (40)$$

The new optimisation equation combines the effects of the thermal storage capacity of the fluid, the convective heat transfer from the walls to the fluid, corrosive properties, and the hydraulic performance characterised by the pumping power. For optimisation of thermophysical and corrosive parameters, eq. 42 was based on the assumption of forced turbulent convection inside a uniformly heated collector tube. In this case, in order to optimise the thermophysical and corrosive properties of HTF, the Reynolds number Re (set according to turbulent regime) and the hydraulic diameter D of the flow channel and its dimensions like length L and correction factor S have been assumed to be constant.

Assuming the heat flux (q''), tube length (L), and the maximum temperature difference between the tube wall and fluid inlet (ΔT_{max}) are fixed, the normalised pumping power is determined by the properties of the fluid and the Reynolds number. To explain the effect of fluid properties on the normalised pumping power without introducing complexity associated with the Reynolds number, the optimisation of the normalised temperature rise (F_N) in eq. 7 is performed:

$$\frac{\partial}{\partial F_N}\left(\frac{1}{F_N^{0.4}(1-F_N)^3}\right) = 0 \tag{41}$$

Substitution of optimised F(= 2/17) into eq. 42 gives

$$\overline{P} \propto \left[\frac{\mu^{1.4}}{\rho^{2.0} c_p^{1.6} k_f^{1.8}}\right]\left[\frac{q''^{2.4}}{\Delta T_{max}^{3.4}}\right]\left[\frac{1}{\left(\frac{N}{\mu\, c_p C_{bulk}}\right)^{0.4}\left(1-\frac{N}{\mu\, c_p C_{bulk}}\right)^3}\right] L^{0.4} \tag{42}$$

At first, a procedure for optimisation based on minimum pumping power $\overline{P}_{min}$ is presented. It can be seen from eq. 42 that $\overline{P}$ is a function of only thermophysical properties: $\frac{\mu^{1.4}}{\rho^{2.0} c_p^{1.6} k^{1.8}}$ and corrosive property: flux N, because other parameters in eq. 42 are either constant or specified. The optimum value of thermophysical parameters: μ or μ_{opt} which gives the minimum value of $\overline{P}$ (or $\overline{P}_{opt}$) can be found from the solution to $\frac{\partial \overline{P}}{\partial \mu} = 0$:

$$\mu_{opt} = \frac{N}{c_p C_{bulk}} \tag{43}$$

Substituting eq. 45 in to eq. 44 and solving gives,

$$\rho_{opt} = \frac{N}{v^3 K_M C_{bulk}} \tag{44}$$

Substituting eq. 45 and 46 in to eq. 44 and eq. 7 and upon solving it gives,

$$c_{p_{opt}} = \frac{K_M^2 C_{bulk}^2}{N^2} \tag{45}$$

Substituting eq. 45, 46, 47 in eq. 4 and eq. 44 and solving it gives,

$$k_{f_{opt}} = \left(\frac{\Delta T_{max}}{Q}\right)^{\frac{1}{2}} \tag{46}$$

Substituting eq. 45 to 48 into eq. 44, and solving it gives,

$$\overline{P}_{min} = \frac{v^3 N^2 Q^{\frac{1}{2}}}{K_M C_{bulk}^2 c_p \Delta T_{max}^{\frac{1}{2}}} \tag{47}$$

Substituting eq. 48 in to eq. 5 for obtaining $\overline{\Delta P}_{min}$

$$\overline{\Delta P}_{opt} = \frac{q'' v^3 N^2 Q^{\frac{1}{2}}}{V K_M C_{bulk}^2 c_p \Delta T_{max}^{\frac{1}{2}}} \tag{48}$$

Table 3. Optimised results for Thermophysical and Corrosive properties of HTF

Optimisation for pumping power $\overline{P}_{min}$	Optimisation for pressure drop $\overline{\Delta P}_{min}$

$\overline{P}_{min} = \frac{v^3 N^2 Q^{\frac{1}{2}}}{K_M\, C_{bulk}^2 c_p\, \Delta T_{max}^{\frac{1}{2}}}$	$\overline{\Delta P}_{min} = \frac{q'' v^3 N^2 Q^{\frac{1}{2}}}{K_M\, C_{bulk}^2 c_p\, \Delta T_{max}^{\frac{1}{2}}}$
$\overline{\Delta P}_{opt} = \frac{q'' v^3 N^2 Q^{\frac{1}{2}}}{V K_M\, C_{bulk}^2 c_p\, \Delta T_{max}^{\frac{1}{2}}}$	$\overline{P}_{opt} = \frac{v^3 N^2 Q^{\frac{1}{2}}}{K_M\, C_{bulk}^2 c_p\, \Delta T_{max}^{\frac{1}{2}}}$
$\mu_{opt} = \frac{N}{c_p C_{bulk} \Delta T_{max}}$	$\mu_{opt} = \frac{2N}{c_p C_{bulk} \Delta T_{max}}$
$\rho_{opt} = \frac{N}{v^3 K_M C_{bulk} \Delta T_{max}}$	$\rho_{opt} = \frac{2N}{v^3 K_M C_{bulk} \Delta T_{max}}$
$c_{p_{opt}} = \frac{K_M^2\, C_{bulk}^2 \Delta T_{max}}{N^2}$	$c_{p_{opt}} = \frac{N^2}{K_M^2\, C_{bulk}^2 \Delta T_{max}}$
$k_{f_{opt}} = \left(\frac{\Delta T_{max}}{Q}\right)^{\frac{1}{2}}$	$k_{f_{opt}} = \left(\frac{\Delta T_{max}}{Q}\right)^{\frac{1}{2}}$

In this case, the specified parameters consist of $\Delta T_{max}, C_{bulk}$ and the minimised parameter is denoted as $\overline{P}$ (red in Table 3), and the optimised parameters include $\mu, \rho, c_p, and\ k_f$. The approach used to minimise pressure drop follows the same procedure as that for minimising pumping power. The outcomes for this scenario are presented in Table 3, along with the results from the minimisation of pumping power. A thorough examination of Table 3 provides us with valuable insights into the fundamental distinctions between optimising for $\bar{P}_{min} and\ \overline{\Delta P}_{min}$ the aim is to minimise pumping power, the optimisation process leads to smaller values for N and v to reduce the flow rate, although at the expense of increased pressure drop, resulting in a lower Reynolds number (Re). In contrast, when the goal is to minimise pressure drop, the method results in relatively larger values for N and v, aimed at reducing pressure drop even if it leads to higher pumping work. It is worth noting that the pumping power $\overline{P}$ is significantly influenced by $\rho\ and\ c_p$, which characterise the fluid's heat storage capacity.

4.2. Optimisation of Reynolds number and Hydraulic diameter of a channel

The optimisation model, discussed in section 3 is used for optimising the pumping power and pressure drop for constant thermophysical and corrosive properties of the fluid. For optimising pumping power and pressure drop, the optimisation focuses on Reynolds number (Re) and hydraulic diameter of a channel, while keeping HTF properties constant. The term constant thermophysical and corrosive properties of HTF means that the HTF is constant i.e. in this case it is water at 40°C therefore all the thermophysical parameters associated with dimensionless pumping load Y are assumed to be constants i.e. fluid density v, fluid viscosity ρ, fluid thermal conductivity K_M, maximum temperature difference b/w wall and fluid ΔT_{max}.

4.2.1. Laminar Regime

The investigation was conducted for the initial optimisation of power required for pumping and the reduction in pressure drop when employing circular channels in a laminar flow condition. Assuming a state of "fully developed flow" from a hydrodynamic perspective, the equation for the friction factor (f) in eq. 9 is provided as follows:

$$f = \frac{64}{R_e} = \frac{64}{\Lambda \bar{D}} \frac{\mu\, c_p}{K_M} \left(\overline{A} - \frac{\Lambda \bar{D}^2}{4 N_u}\right) \tag{49}$$

and the Nusselt number in eq. 10 is constant (Nu = 4.363) for constant heat flux.

Initially, an optimisation procedure is introduced, centered on minimising the required pumping energy. By substituting eqs. 8 and 42 into eq. 4, the dimensionless pumping energy can be represented as follows.

$$\overline{P} = \frac{32\Lambda^2}{\overline{Pr}^2} \cdot \frac{\overline{A}}{\overline{D}^2 \cdot \left(\overline{A} - \frac{\Lambda \overline{D}^2}{4Nu}\right)^2} \tag{50}$$

Now $\overline{P}$ is a function of only $\overline{D}^2$ because other parameters are either constant or specified. The optimum value of $\overline{D}$ (or $\overline{D}_{opt}$) which gives the minimum value of $\overline{P}$ (or $\overline{P}_{opt}$) can be found from the solution to $\frac{\partial \overline{P}}{\partial \overline{D}} = 0$:

$$\overline{D}_{opt} = \left(\frac{4N_u \overline{A}}{3\Lambda}\right)^{\frac{1}{2}} \tag{51}$$

By substituting eq. 44 into eq. 8, an optimal Reynolds number is derived to minimise pumping power.

$$Re_{opt} = 1/Pr \left(\frac{3\Lambda Nu}{\overline{A}}\right)^{\frac{1}{2}} \tag{52}$$

The minimum value of the pumping power is obtained by substituting eq. 44 into eq. 43.

$$\overline{P}_{min} = \frac{54\Lambda^3}{\overline{Pr}^2 Nu \overline{A}^2} \tag{53}$$

The pressure drop at the optimum condition is found by substituting eq. 42, 44, and 45 in ΔP in eq. 5, where ΔP has been normalised first to $\overline{\Delta P}$

$$\overline{\Delta P}_{opt} = \frac{36\Lambda^2}{Pr\, Nu \overline{A}^2} \tag{54}$$

In this instance, the specified parameters comprise Λ and $\overline{A}$, with the parameter to minimise being $\overline{P}$ (red in Table 4), and the parameters to optimise being $\overline{D}$ and Re. The approach for reducing pressure drop follows the same steps as minimising pumping power. The findings for this particular scenario can be found in Table 4, alongside the outcomes for minimising pumping power. A thorough examination of Table 4 provides insight into the fundamental distinctions between optimising for $\overline{P}_{min}$ and $\overline{\Delta P}_{min}$. When striving to minimise pumping power, the optimisation process results in smaller values for $\overline{D}$ to decrease the flow rate, although at the expense of higher pressure drop, consequently leading to lower Re. Conversely, when the goal is to minimise pressure drop, the method yields relatively larger values for $\overline{D}$ to reduce pressure drop, even though this requires increased pumping work, ultimately resulting in higher Re.

Table 4. Optimised results for laminar regime

Optimisation for pumping power $\overline{P}_{min}$	Optimisation for pressure drop $\overline{\Delta P}_{min}$
$\overline{P}_{min} = \frac{54\Lambda^3}{\overline{Pr}^2 Nu \overline{A}^2}$	$\overline{\Delta P}_{min} = \frac{32\Lambda^2}{Pr Nu \overline{A}^2}$
$\overline{\Delta P}_{opt} = \frac{36\Lambda^2}{Pr\, Nu \overline{A}^2}$	$\overline{P}_{opt} = \frac{64\Lambda^3}{\overline{Pr}^2 Nu \overline{A}^2}$
$\overline{D}_{opt} = \left(\frac{4N_u \overline{A}}{3\Lambda}\right)^{\frac{1}{2}}$	$\overline{D}_{opt} = \left(\frac{2\Lambda Nu}{\overline{A}}\right)^{\frac{1}{2}}$
$Re_{opt} = 1/Pr \left(\frac{3\Lambda Nu}{\overline{A}}\right)^{\frac{1}{2}}$	$Re_{opt} = 2/Pr \left(\frac{2\Lambda Nu}{\overline{A}}\right)^{\frac{1}{2}}$

4.2.2. Turbulent Regime

For the case of fully developed turbulent flow in a smooth circular channel, the following formulae for the friction factor and Nusselt number are accurate for a wide range of Re.

$$\mathrm{f} = (0.790 \ln \mathrm{Re} - 1.64)^{-2} \qquad 10^4 < \mathrm{Re} < 5\,\mathrm{x}10^6 \tag{55}$$

and,

$$\mathrm{Nu} = \frac{\left(\frac{\mathrm{f}}{8}\right)(\mathrm{Re}-1000)\mathrm{Pr}}{1+12.7\left(\frac{\mathrm{f}}{8}\right)^{\frac{1}{2}}\left(\mathrm{Pr}^{\frac{2}{3}}-1\right)} \quad 3000 < \mathrm{Re} < 10^6, \mathrm{Pr} > 0.5) \tag{56}$$

By substituting eq. 48 into eq. 49, the Nu can be expressed as a function of only Re because the properties of the HTF are assumed constant.

Eq. 8 can be solved for as,

$$\overline{\mathrm{D}} = \left(\frac{2\mathrm{Nu}}{\mathrm{RePr}}\right)^2 + \frac{4\mathrm{Nu}\overline{\mathrm{A}}}{\Lambda} - \frac{2\mathrm{Nu}}{\mathrm{RePr}} \tag{57}$$

Since both $\overline{\mathrm{A}}$ and Λ have been specified and Pr is constant, D can be expressed as a function of Re only by substituting eq. 48 into eq. 49. Further, because both $\overline{\mathrm{P}}$ and $\overline{\Delta \mathrm{P}}$ are functions of f, D, and Re [see eq. 4 and eq. 5], they can be expressed in terms of by substituting eq. 48 and eq. 50 into them.

As both $\overline{\mathrm{A}}$ and Λ have been defined, and $\mathrm{P_r}$ remains constant, D can be formulated solely as a function of Re by replacing eq. 48 with eq. 49. Additionally, since both $\overline{\mathrm{P}}$ and $\overline{\Delta \mathrm{P}}$ are dependent on f, D, and Re (as seen in eq. 4 and eq. 5), they can be expressed in relation to them by substituting eq. 48 and eq. 50 into these expressions.

As for the case of minimisation of the pumping power, the $\overline{\mathrm{P}}_{\mathrm{min}}$ is obtained from $\frac{\partial \overline{\mathrm{P}}}{\partial \overline{\mathrm{D}}} = 0$, or

$$\frac{3}{2} - \frac{\mathrm{Re}}{\mathrm{F}} \cdot \frac{\partial \mathrm{F}}{\partial \mathrm{Re}} - \frac{2\mathrm{Re}}{\overline{\mathrm{D}}} \cdot \frac{\partial \overline{\mathrm{D}}}{\partial \mathrm{Re}} = 0 \tag{58}$$

Here F = 0.79ln Re-1.64. This equation can be readily solved numerically for $\mathrm{Re}_{\mathrm{opt}}$. Once Re_{opt} is obtained, one can obtain $\overline{\mathrm{D}}_{opt}$ from eq. 50, $\overline{\mathrm{P}}_{min}$ from eq. 4, and $\Delta\overline{\mathrm{P}}_{opt}$ from eq. 5.

Alternatively, in the context of optimising for minimal pressure drop, $\overline{\Delta \mathrm{P}}_{\mathrm{min}}$ can be achieved by solving the equation $\frac{\partial \overline{\Delta \mathrm{P}}_{\mathrm{min}}}{\partial \mathrm{Re}} = 0$, where:

$$1 - \frac{\mathrm{Re}}{\mathrm{F}} \cdot \frac{\partial \mathrm{F}}{\partial \mathrm{Re}} - \frac{3\mathrm{Re}}{2\overline{\mathrm{D}}} \cdot \frac{\partial \overline{\mathrm{D}}}{\partial \mathrm{Re}} = 0 \tag{59}$$

In this case, after this equation is solved for $\mathrm{Re}_{\mathrm{opt}}$, one can obtain $\overline{\mathrm{D}}_{\mathrm{opt}}$ from eq. 50, $\overline{\Delta \mathrm{P}}_{\mathrm{min}}$ from eq. 5, $\overline{\mathrm{P}}_{\mathrm{opt}}$ from eq. 4.

5. Results and Discussion

5.1. Results of Thermophysical and Corrosive properties of HTF

With the optimisation scheme introduced in the previous sections, several important relationships among the parameters will be presented. Fig. 4 shows the trends for various thermophysical and corrosive

parameters such as $\overline{P}_{min}$, $\overline{\Delta P}_{opt}$, ρ_{opt}, μ_{opt}, $c_{p_{opt}}$, $k_{f_{opt}}$ versus ΔT. In the figure, the optimisation of parameters $\mu, \rho, c_p, and\ k_f$ result in the minimisation of the pumper power $\overline{P}_{min}$ and pressure drop $\overline{\Delta P}_{opt}$. These parameters are represented by their respective trends in the fig. 4. The trends for the $\overline{P}_{min}$ and $\overline{\Delta P}_{opt}$ show that the pumping power and pressure drop are minimised due to optimisation of parameters ρ_{opt}, μ_{opt}, $c_{p_{opt}}$, $k_{f_{opt}}$. It is worth noting that the pumping power $\overline{P}_{min}$ pressure drop $\overline{\Delta P}_{opt}$ are significantly influenced by the reduction of fluid density ρ_{min} and increase in specific heat capacity $c_{p_{opt}}$ due to optimsation. Further the optimisation of thermal conductivity k_{opt} and dynamic viscosity μ_{opt} reduces the pumping power and pressure drop.

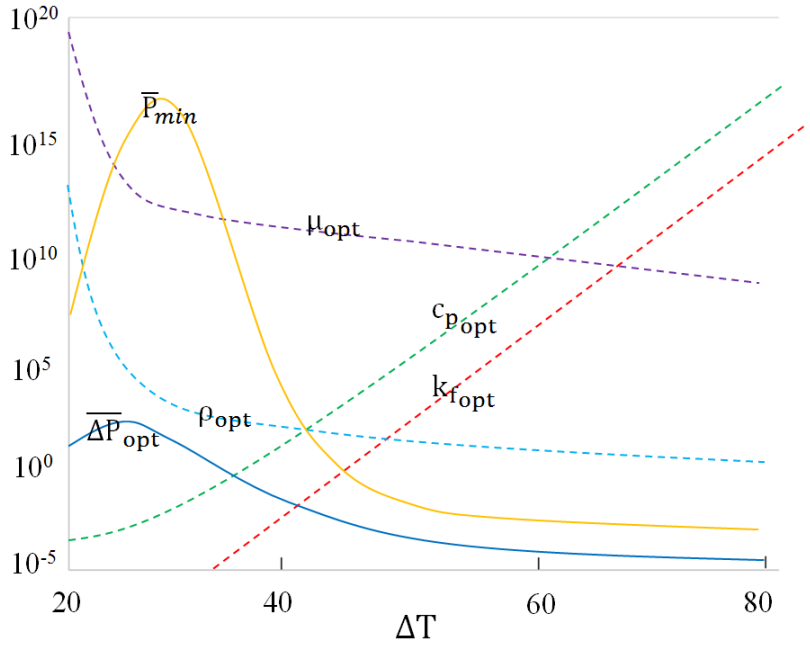

Figure 4. Figure showing $\overline{P}_{min}$, $\overline{\Delta P}_{opt}$, ρ_{opt}, μ_{opt}, $c_{p_{opt}}$, $k_{f_{opt}}$ versus ΔT.

5.2. Results of Reynolds number and Hydraulic diameter of a channel

By implementing the optimisation plan outlined in Section 4, significant connections among the parameters were unveiled. In the subsequent sections, water is utilised as the HTF at a temperature of 40 ^{o}C, with $\overline{A}$ held constant at 0.3. All calculations and results pertain to the scenario of minimising pumping power unless explicitly specified otherwise.

5.2.1. Laminar Regime

Fig. 5 illustrates the correlation between Re (Reynolds number) and Λ (a dimensionless parameter) for laminar flow conditions. The Reynolds number range chosen for this analysis is $0 < Re < 2300$. Within this figure, solid lines depict the relationship between Re and the average pumping power ($\overline{P}$) at different values of Λ, namely, $10^4, 10^5, 10^6, 10^7, 10^8, and\ 10^9$, arranged from bottom to top, respectively. A dotted line represents the locus of Re_{opt} (the optimum Reynolds number) versus $\overline{P}_{min}$ (the minimum average pumping power). It is evident that as Λ increases, both $\overline{P}$ and Re_{opt} also, increase. This graphical representation clearly demonstrates the presence of an optimal Reynolds number that minimises the required pumping power.

Moving on to Fig. 6, it presents the dependency of key parameters, namely $\overline{P}_{min}$, $\overline{D}_{opt}$ (optimum hydraulic diameter), and $\overline{\Delta P}_{opt}$ (optimum pressure drop), on the thermal load Λ. In this figure, only Λ values that result in $0 < Re_{opt} < 2300$ are considered. The Λ values leading to $Re_{opt} = 2300$ are excluded from this analysis since, in such cases, $\overline{P}$ exhibits a continuous decrease with increasing Reynolds number. It can be seen that as Λ increases, $\overline{P}_{min}$, $\overline{\Delta P}_{opt}$, N_{opt}, Re_{opt} increase while $\overline{D}_{opt}$ decreases. The increase

in $\overline{P}_{min}$ and $\overline{\Delta P}_{opt}$ clearly indicates the pumping power and pressure drop are directly influenced by thermal load Λ.

5.2.2. Turbulent Regime

In Fig. 7, the correlation between Re and $\overline{P}$ can be observed, which resembles Fig. 5. The solid lines in the graph represent Re versus $\overline{P}$ at Λ values of $10^4, 10^5, 10^6, 10^7, 10^8, and\ 10^9$, arranged from bottom to top. Meanwhile, the dotted line represents the locus of Re_{opt} versus $\overline{P}_{min}$. In this scenario, Re_{opt} maintains a constant value of 3000, which is the lower boundary of Re, when Λ remains relatively low. As Λ increases, there is a clear indication in figure that both the average pumping power $\overline{P}_{min}$ and the optimum Reynolds number Re_{opt} also experience an increase.

Fig. 8 is similar to Fig. 6, but it pertains to the turbulent regime. Only Λ values resulting in $3000 < Re_{opt} < 10^6$ are considered. Once Re_{opt} reaches 10^6, the calculation ceases. In contrast to the laminar case, each line exhibits a variation in its gradient. Fig. 9 shows the comparison of Λ versus $\overline{P}_{min}$ relation between laminar flow and turbulent flow when $\overline{A}$ = 0:3 and the working fluid is water at 40 °C. As Λ rises, there is a noticeable increase in $\overline{P}_{min}$, $\overline{\Delta P}_{opt}$, N_{opt}, Re_{opt}, accompanied by a decrease in $\overline{D}_{opt}$. This observed escalation in $\overline{P}_{min}$ and $\overline{\Delta P}_{opt}$ distinctly signifies the direct impact of thermal load Λ on both pumping power and pressure drop.

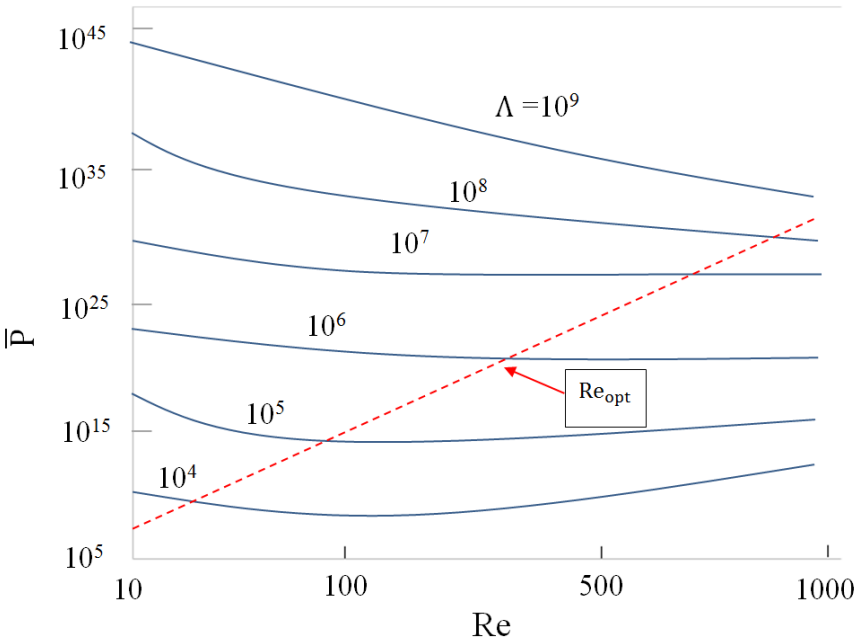

Figure 5. The solid lines represent Re versus $\overline{P}$ at $\Lambda = 10^2, 10^3, 10^4, 10^5, 10^6$, and 10^7. The dotted line denotes a locus of the Re_{opt} versus $\overline{P}_{min}$

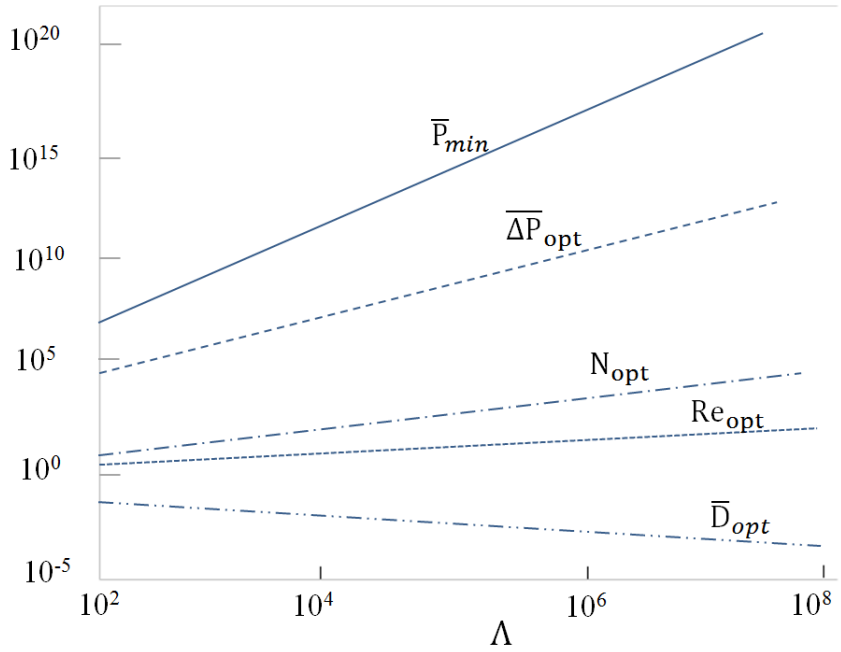

Figure 6. Figure showing $\overline{P}_{min}$, $\overline{\Delta P}_{opt}$, N_{opt}, Re_{opt}, $\overline{D}_{opt}$ versus Λ in case of laminar flow (Re < 2300): $\overline{A}$ = 0:3 and work fluid is water at 40°C.

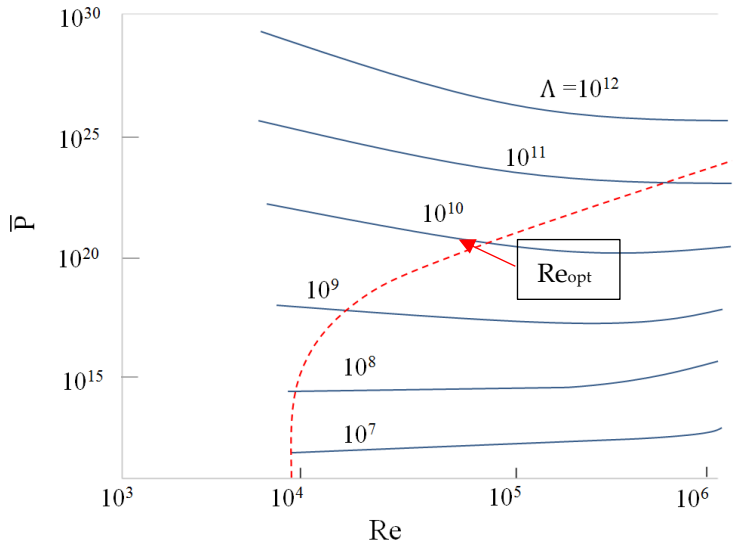

Figure 7. Relationship between Re and for turbulent flow (3000 < Re < 10) with = 10^{12}, 10^{11}, 10^{10}, 10^{9}, 10^{8}, 10^{7} from bottom to top, respectively. The dotted line denotes a locus of Re_{opt} versus $\overline{P}_{min}$. $\overline{A}$ = 0:3 and the working fluid is water at 40 °C.

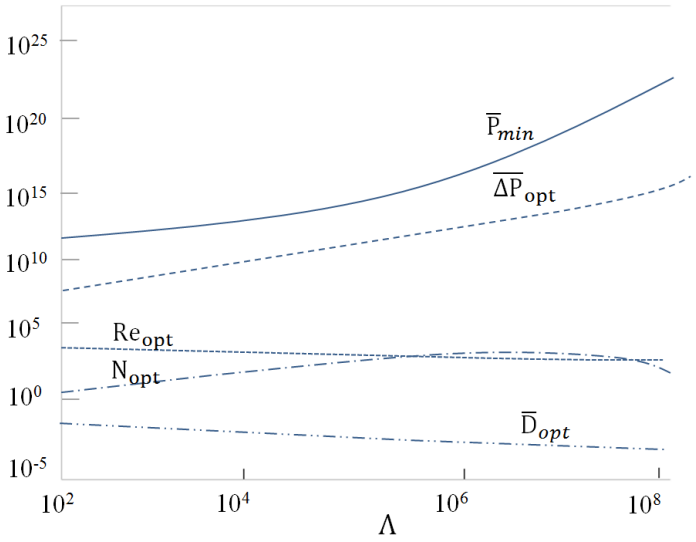

Figure 8. Figure showing $\overline{P}_{min}$, $\overline{\Delta P}_{opt}$, N_{opt}, Re_{opt}, $\overline{D}_{opt}$ versus Λ in case of turbulent flow ($3000 < Re < 10^6$): $\overline{A}$ = 0:3 and work fluid is water at 40°C.

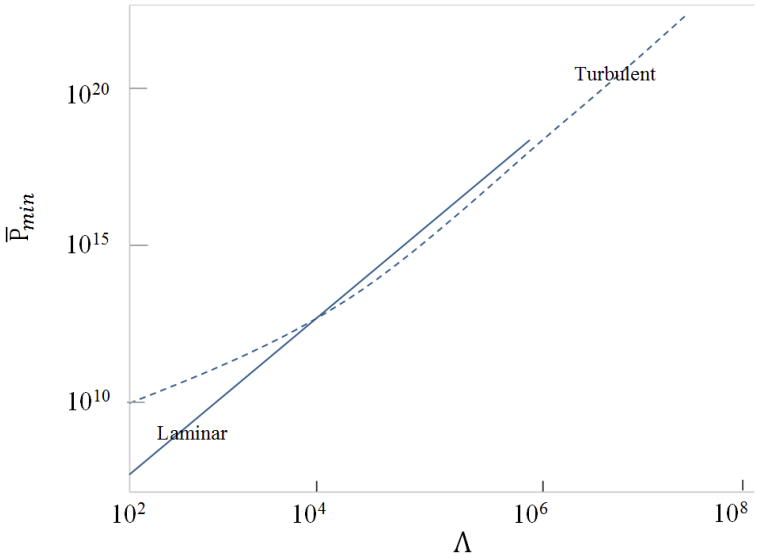

Figure 9. Comparison of Λ versus $\overline{P}_{min}$ relation between laminar flow and turbulent flow: $\overline{A}$ = 0:3 and working fluid is water at 40 °C.

6. Validation of New Optimisation Model

In order to validate the accuracy of the developed optimisation model, selected HTFs (shown in Table 5 from the previous Section 2) were used to simulate their properties through the newly developed optimisation model presented in Section 3. The observed trends in pumping power minimisation, as related to the optimization of parameters such as density, specific heat capacity, thermal conductivity, and dynamic viscosity, align with findings from Vivel et al [68], Paul et al [69] .

Table 5. Conventional and potential HTFs for solar collector fields.

		Heat Transfer Fluid
Oils	Synthetic	Therminol® VP-1
	Mineral	Caloria HT 43
Molten salts	Nitrates	Hitec®, Hitec® Solar Salt
	Chlorides	MgCl2-KCl
	Fluorides	LiF-NaF-KF (FLiNaK)
Other liquids		Mercury
		Water
Pressurised gases		Water vapor (30 - 100 bar)
		Air (30-100 bar)

Fig.10 shows the thermophysical properties and the pumping power efficiency N_{Eff} of the various HTFs listed in Table 5. These fluids have been selected to analyse their performance by using a new optimisation model. Volumetric heat capacity (Fig. 10a), thermal conductivity (Fig. 10b), and dynamic viscosity (Fig. 10c) corrosion rate (Fig. 10d) values are shown, and the combined effects of these properties (Fig. 10e) are evaluated using the new optimisation model discussed in previous section 3.

In the evaluation of HTFs, synthetic oil outperforms mineral oil due to its higher thermal conductivity (fig. 10c) and lower viscosity (fig. 10a). However, Therminol® VP-1, commonly used, limits efficiency due to its low thermal breakdown temperature. Molten salts, like Hitec® Solar Salt, excel with higher pumping power efficiency, outperforming oils, and even fluoride salts at very high temperatures (fig. 10e). Yet, their high freezing point necessitates costly freeze protection measures. Water and water vapour offer promise for solar thermal plants and have been successfully employed in the DISS project. Gases, like air, boast low viscosity and cost but may increase piping expenses with elevated pressure.

Operating temperature significantly impacts fluid performance. Liquids benefit from higher temperatures due to reduced viscosity (fig. 10a), while gases experience diminishing efficiency as temperature rises (fig. 10b). Elevated outlet temperatures boost power cycle efficiency, but thermal stability and coating limitations set constraints. Selective coatings rated up to ~450°C could expand possibilities.

Safety and reliability are critical considerations. Flammable fluids demand fire protection, exemplified by the SEGS plant switch from mineral to synthetic oil. Mercury, though efficient, is toxic and not recommended. Molten salt systems require corrosion-resistant materials at high temperatures (fig. 10d). Careful fluid selection is essential for safe and dependable solar plant operation.

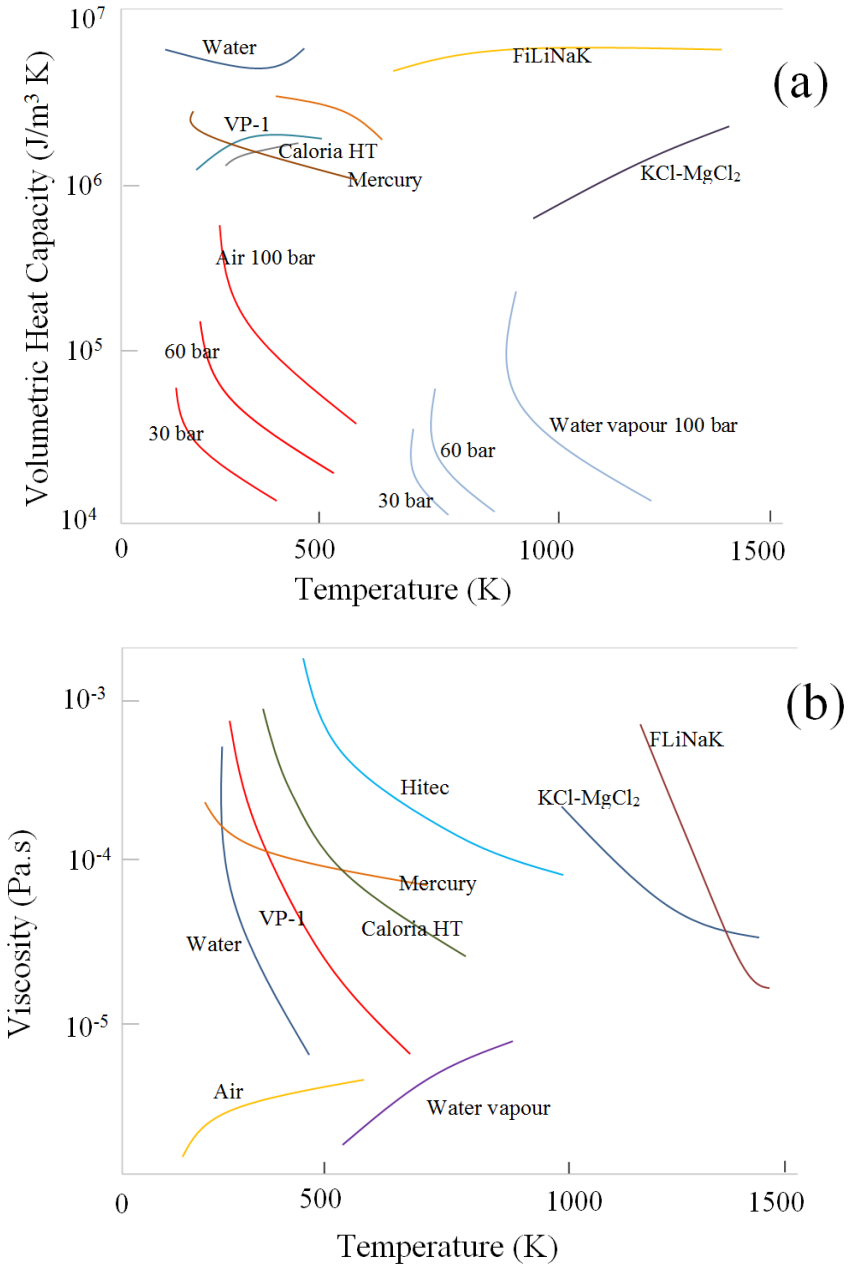
(a)
Volumetric Heat Capacity (J/m³ K)
10⁷
10⁶
10⁵
10⁴
Water
FiLiNaK
VP-1
Caloria HT
Mercury
KCl-MgCl₂
Air 100 bar
60 bar
30 bar
Water vapour 100 bar
60 bar
30 bar
0
500
1000
1500
Temperature (K)
(b)
Viscosity (Pa.s)
10-3
10-4
10-5
FLiNaK
Hitec
KCl-MgCl₂
Mercury
VP-1
Caloria HT
Water
Air
Water vapour
0
500
1000
1500
Temperature (K)

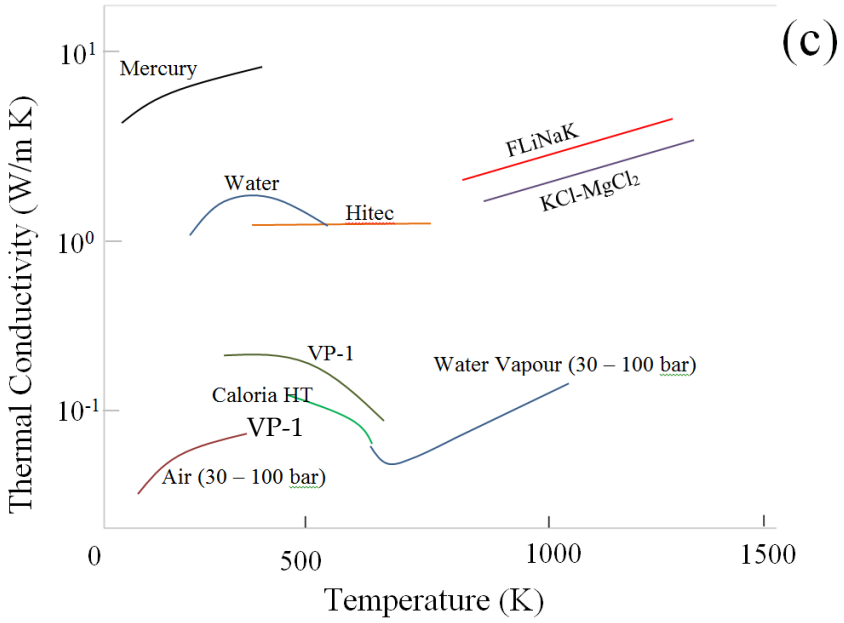
(c)
Thermal Conductivity (W/m K)
10^1
10^0
10^{-1}
Mercury
Water
Hitec
FLiNaK
KCl-MgCl₂
VP-1
Caloria HT
VP-1
Water Vapour (30 – 100 bar)
Air (30 – 100 bar)
0
500
1000
1500
Temperature (K)

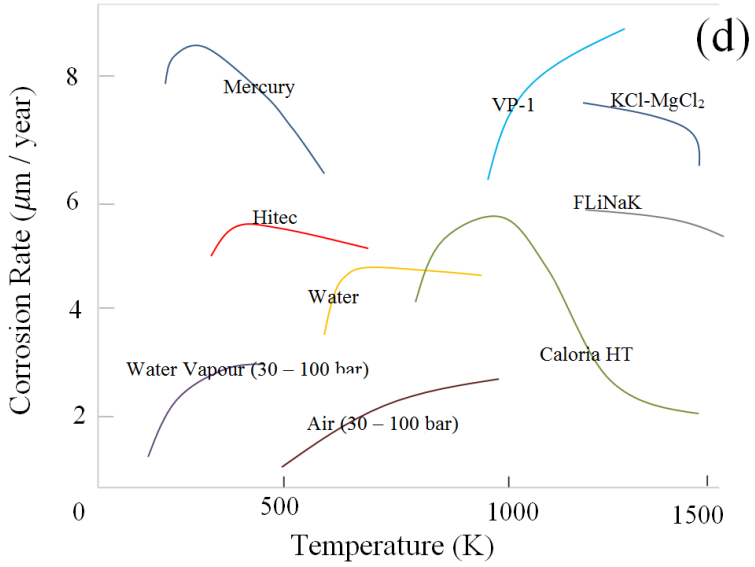
(d)
Corrosion Rate (μm / year)
8
6
4
2
0
Mercury
VP-1
KCl-MgCl₂
Hitec
FLiNaK
Water
Caloria HT
Water Vapour (30 – 100 bar)
Air (30 – 100 bar)
500
1000
1500
Temperature (K)

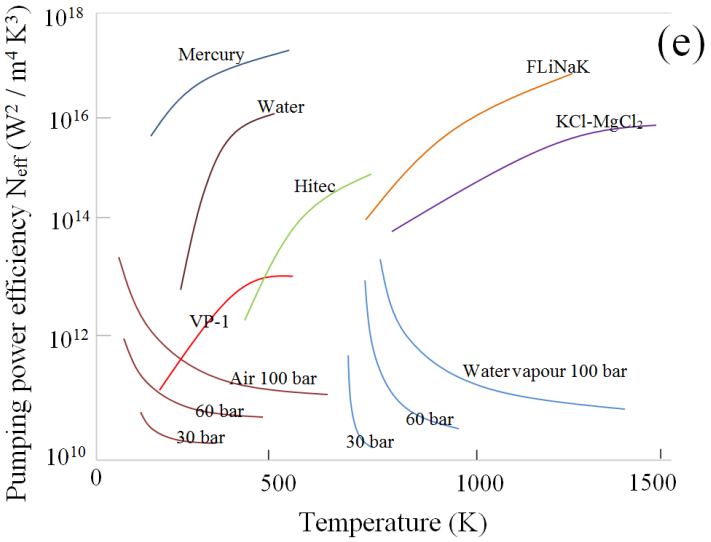

Figure 10. Thermophysical properties and pumping power efficiency of HTFs: (a) volumetric heat capacity, (b) dynamic viscosity, (c) thermal conductivity, (d) Corrosion rate, (e) pumping power efficiency new optimisation model Pl = Psat (T) and Pg = 30 – 100 bar.

7. Conclusions

In this study, an innovative numerical optimisation framework is developed to enhance the thermal efficiency of thermo-fluids while minimising pumping energy consumption in concentrated solar power systems. The model integrates both thermophysical and corrosive modeling of heat transfer fluids (HTFs), acknowledging the crucial role of fluid properties and corrosive behavior in fluid performance. By optimising parameters such as thermophysical properties, Reynolds number, and channel dimensions, the model establishes a governing principle for optimising concentrated solar power systems.

The results demonstrate significant improvements in pumping power and pressure drop through optimisation strategies, particularly by minimising fluid density and maximising specific heat capacity. Furthermore, the study reveals the presence of optimal Reynolds numbers that minimise pumping power under both laminar and turbulent flow conditions.

Validation of the optimisation model was conducted using selected HTFs, with results indicating superior performance of synthetic oils and molten salts in terms of pumping power efficiency. However, considerations such as thermal stability, freezing point, safety, and reliability play crucial roles in the selection of HTFs for solar thermal applications.

Overall, this research provides valuable insights into the optimisation of thermo-fluid systems in concentrated solar power, paving the way for more efficient and sustainable solar energy utilisation. Future studies could further explore the application of the developed optimisation framework in practical solar thermal systems and investigate additional factors influencing fluid performance and system efficiency.

Appendix

Nomenclature

A area (m^2)
C_k coefficient of k enhancement ($Wm^{-1}K^{-1}$)
C_p specific heat capacity at constant pressure ($Jkg^{-1}K^{-1}$)
C_μ coefficient of μ enhancement ($kgm^{-1}s^{-1}$ or Pa s)
d particle diameter (nm)
D diameter (m)
E heat transfer enhancement factor
F_r Froude number g gravitational acceleration (ms^{-2})
G Total mass flux through a tube ($kgm^{-2}s^{-1}$)
h heat transfer coefficient ($Wm^{-2}K^{-1}$),

K	permeability (m^2)
k	thermal conductivity ($Wm^{-1}K^{-1}$)
L	length (m)
m"	mass flux ($kgm^{-2}s^{-1}$)
M	two-phase flow pressure drop multiplier
Nu	Nusselt number
N_i	Species Flux (or N)
p	perimeter (m)
P	pressure (Pa)
P_r	Prandtl number
q"	heat flux (Wm^{-2})
r	radius (m)
Re	Reynolds number
S	heat transfer correction factor
T	temperature (K)
u	velocity (ms^{-1})
V	averaged bulk velocity (ms^{-1})
ν	kinematic viscosity (m2/s)
Λ	dimensionless thermal load
Φ	volume fraction of solid phase
ρ	density (kgm^{-3})
θ	angle (º)
β	tilt angle (º)
μ	dynamic viscosity ($kgm^{-1}s^{-1}$)
α	thermal diffusivity (m^2s^{-1})
x	vapor quality
Y	dimensionless pumping load
$\overline{P}_{min}$	minimum average pumping power
$\overline{\Delta P}_{opt}$	pressure drop at the optimum condition

References

1. Vutukuru, R., A.S. Pegallapati, and R. Maddali, *Suitability of various heat transfer fluids for high temperature solar thermal systems.* Applied Thermal Engineering, 2019. **159**: p. 113973.
2. Nazir, M., Z.A. Khan, and K. Stokes, *A holistic mathematical modelling and simulation for cathodic delamination mechanism–a novel and an efficient approach.* Journal of Adhesion Science and Technology, 2015. **29**(22): p. 2475-2513.
3. Nazir, M., et al., *A predictive model for life assessment of automotive exhaust mufflers subject to internal corrosion failure due to exhaust gas condensation.* Engineering Failure Analysis, 2016. **63**: p. 43-60.
4. Tyagi, H., P. Phelan, and R. Prasher, *Predicted efficiency of a low-temperature nanofluid-based direct absorption solar collector*. 2009.
5. Eastman, J.A., et al., *Anomalously increased effective thermal conductivities of ethylene glycol-based nanofluids containing copper nanoparticles.* Applied physics letters, 2001. **78**(6): p. 718-720.
6. Tiznobaik, H. and D. Shin, *Enhanced specific heat capacity of high-temperature molten salt-based nanofluids.* International Journal of Heat and Mass Transfer, 2013. **57**(2): p. 542-548.
7. Vignarooban, K., et al., *Heat transfer fluids for concentrating solar power systems – A review.* Applied Energy, 2015. **146**: p. 383-396.
8. Pacio, J. and T. Wetzel, *Assessment of liquid metal technology status and research paths for their use as efficient heat transfer fluids in solar central receiver systems.* Solar Energy, 2013. **93**: p. 11-22.

9. Liu, M., et al., *Impact of the heat transfer fluid in a flat plate phase change thermal storage unit for concentrated solar tower plants.* Solar Energy, 2014. **101**: p. 220-231.
10. Tian, Y. and C.-Y. Zhao, *A review of solar collectors and thermal energy storage in solar thermal applications.* Applied Energy, 2013. **104**: p. 538-553.
11. Zunft, S., et al., *Jülich solar power tower—experimental evaluation of the storage subsystem and performance calculation.* Journal of Solar Energy Engineering, 2011. **133**(3): p. 031019.
12. Avila-Marin, A.L., *Volumetric receivers in solar thermal power plants with central receiver system technology: a review.* Solar energy, 2011. **85**(5): p. 891-910.
13. Meier, G., *A review of advances in high-temperature corrosion.* Materials Science and Engineering: A, 1989. **120**: p. 1-11.
14. Klöwer, J., *High temperature Corrosion behaviour of iron aluminides and iron‐aluminium‐chromium alloys.* Materials and Corrosion, 1996. **47**(12): p. 685-694.
15. Chen, R. and W. Yeun, *Review of the high-temperature oxidation of iron and carbon steels in air or oxygen.* Oxidation of metals, 2003. **59**(5-6): p. 433-468.
16. Chen, R. and W. Yuen, *Oxide-scale structures formed on commercial hot-rolled steel strip and their formation mechanisms.* Oxidation of metals, 2001. **56**(1-2): p. 89-118.
17. Birnbaum, J., et al., *Steam temperature stability in a direct steam generation solar power plant.* Solar Energy, 2011. **85**(4): p. 660-668.
18. Modi, A. and F. Haglind, *Performance analysis of a Kalina cycle for a central receiver solar thermal power plant with direct steam generation.* Applied Thermal Engineering, 2014. **65**(1): p. 201-208.
19. Feldhoff, J.F., et al., *Economic potential of solar thermal power plants with direct steam generation compared with HTF plants.* Journal of Solar Energy Engineering, 2010. **132**(4): p. 041001.
20. Pistocchini, L. and M. Motta, *Feasibility study of an innovative dry-cooling system with phase-change material storage for concentrated solar power multi-MW size power plant.* Journal of Solar Energy Engineering, 2011. **133**(3): p. 031010.
21. Gil, A., et al., *State of the art on high temperature thermal energy storage for power generation. Part 1—Concepts, materials and modellization.* Renewable and Sustainable Energy Reviews, 2010. **14**(1): p. 31-55.
22. Dunn, R.I., P.J. Hearps, and M.N. Wright, *Molten-salt power towers: newly commercial concentrating solar storage.* Proceedings of the IEEE, 2012. **100**(2): p. 504-515.
23. Hammad Nazir, M., et al., *Analyzing and modelling the corrosion behavior of Ni/Al2O3, Ni/SiC, Ni/ZrO2 and Ni/Graphene nanocomposite coatings.* Materials, 2017. **10**(11): p. 1225.
24. Ding, W., et al., *Electrochemical measurement of corrosive impurities in molten chlorides for thermal energy storage.* Journal of Energy Storage, 2018. **15**: p. 408-414.
25. Kenisarin, M.M., *High-temperature phase change materials for thermal energy storage.* Renewable and sustainable energy reviews, 2010. **14**(3): p. 955-970.
26. Wei, G., et al., *Selection principles and thermophysical properties of high temperature phase change materials for thermal energy storage: A review.* Renewable and Sustainable Energy Reviews, 2018. **81**: p. 1771-1786.
27. Khan, Z.A., M. Grover, and M.H. Nazir. *The implications of wet and dry turning on the surface quality of EN8 steel*. in *Transactions on Engineering Technologies: World Congress on Engineering 2014*. 2015. Springer.
28. Becker, M., *Comparison of heat transfer fluids for use in solar thermal power stations.* Electric Power Systems Research, 1980. **3**(3-4): p. 139-150.
29. Mouromtseff, I., *Water and forced-air cooling of vacuum tubes nonelectronic problems in electronic tubes.* Proceedings of the IRE, 1942. **30**(4): p. 190-205.

30. Bonilla, C.F., *Nuclear engineering.* 1957.
31. Murakami, Y. and B.B. Mikic, *Parametric optimization of multichanneled heat sinks for VLSI chip cooling.* IEEE Transactions on Components and Packaging Technologies, 2001. **24**(1): p. 2-9.
32. Lenert, A., Y. Nam, and E.N. Wang, *Heat transfer fluids.* Annual Review of Heat Transfer, 2012. **15**(15).
33. Nazir, M., Z. Khan, and K. Stokes, *Modelling of metal-coating delamination incorporating variable environmental parameters.* Journal of Adhesion Science and Technology, 2015. **29**(5): p. 392-423.
34. Nazir, M.H., et al., *Experimental analysis and modelling for reciprocating wear behaviour of nanocomposite coatings.* Wear, 2018. **416**: p. 89-102.
35. Hetsroni, G., et al., *Heat transfer in micro-channels: Comparison of experiments with theory and numerical results.* International Journal of Heat and Mass Transfer, 2005. **48**(25-26): p. 5580-5601.
36. Axworthy, D.H., M.S. Ghidaoui, and D.A. McInnis, *Extended thermodynamics derivation of energy dissipation in unsteady pipe flow.* Journal of Hydraulic Engineering, 2000. **126**(4): p. 276-287.
37. Salman, B., et al., *Characteristics of heat transfer and fluid flow in microtube and microchannel using conventional fluids and nanofluids: a review.* Renewable and Sustainable Energy Reviews, 2013. **28**: p. 848-880.
38. Bergman, T.L., et al., *Fundamentals of heat and mass transfer.* John Wiley & Sons, 2011. **384**: p. 385.
39. Mills, A. and D. Chung, *Heat transfer across turbulent falling films.* International Journal of Heat and Mass Transfer, 1973. **16**(3): p. 694-696.
40. Nazir, M., et al., *Modeling the effect of residual and diffusion-induced stresses on corrosion at the interface of coating and substrate.* Corrosion, 2016. **72**(4): p. 500-517.
41. Nazir, M., Z.A. Khan, and K. Stokes, *Optimisation of interface roughness and coating thickness to maximise coating–substrate adhesion–a failure prediction and reliability assessment modelling.* Journal of Adhesion Science and Technology, 2015. **29**(14): p. 1415-1445.
42. Nazir, M.H., A. Saeed, and Z. Khan, *A comprehensive predictive corrosion model incorporating varying environmental gas pollutants applied to wider steel applications.* Materials Chemistry and Physics, 2017. **193**: p. 19-34.
43. Incropera, F.P., et al., *Principles of heat and mass transfer*. 2013: Wiley.
44. Deen, W.M., *Analysis of transport phenomena (topics in chemical engineering)*. Vol. 3. 1998: Oxford University Press, New York.
45. Latif, J., et al., *An optimal condition based maintenance scheduling for metal structures based on a multidisciplinary research approach.* Structure and Infrastructure Engineering, 2019. **15**(10): p. 1366-1381.
46. Saeed, A., Z.A. Khan, and M.H. Nazir, *Time dependent surface corrosion analysis and modelling of automotive steel under a simplistic model of variations in environmental parameters.* Materials Chemistry and Physics, 2016. **178**: p. 65-73.
47. Garcia-Diaz, B.L., et al. *Electrochemical study of corrosion in high temperature molten salts*. in *Meeting Abstracts*. 2014. The Electrochemical Society.
48. Tedmon, C., D. Vermilyea, and J. Rosolowski, *Intergranular corrosion of austenitic stainless steel.* Journal of the Electrochemical Society, 1971. **118**(2): p. 192-202.
49. Loria, E.A., *Perspective on Intergranular Corrosion of Type 304 Stainless Steel.* JOM, 1982. **34**(10): p. 16-22.
50. Pan, Y.-M., et al., *Grain-boundary chemistry and intergranular corrosion in alloy 825.* Metallurgical and Materials Transactions A, 2000. **31**(4): p. 1163-1173.
51. Park, J.H., et al., *Three-dimensional atom probe analysis of intergranular segregation and precipitation behavior in Ti–Nb-stabilized low-Cr ferritic stainless steel.* Scripta materialia, 2013. **68**(5): p. 237-240.
52. Olson, L., et al., *Nickel-plating for active metal dissolution resistance in molten fluoride salts.* Journal of Nuclear Materials, 2011. **411**(1): p. 51-59.

53. Nazir, M. and Z.A. Khan, *A review of theoretical analysis techniques for cracking and corrosive degradation of film-substrate systems.* Engineering Failure Analysis, 2017. **72**: p. 80-113.
54. Bajwa, R., et al., *Wear and friction properties of electrodeposited Ni-based coatings subject to nano-enhanced lubricant and composite coating.* Acta Metallurgica Sinica (English Letters), 2016. **29**: p. 902-910.
55. Nazir, M., Z.A. Khan, and K. Stokes, *A unified mathematical modelling and simulation for cathodic blistering mechanism incorporating diffusion and fracture mechanics concepts.* Journal of Adhesion Science and Technology, 2015. **29**(12): p. 1200-1228.
56. Cao, L., et al., *Towards understanding the nanofluidic reverse electrodialysis system: well matched charge selectivity and ionic composition.* Energy & Environmental Science, 2011. **4**(6): p. 2259-2266.
57. Nazir, M., Z.A. Khan, and K. Stokes, *Analysing the coupled effects of compressive and diffusion induced stresses on the nucleation and propagation of circular coating blisters in the presence of micro-cracks.* Engineering Failure Analysis, 2016. **70**: p. 1-15.
58. Newman, J. and K.E. Thomas-Alyea, *Electrochemical systems*. 2012: John Wiley & Sons.
59. Presuel-Moreno, F., et al., *Computational Modeling of Active Corrosion Inhibitor Release from an Al-Co-Ce Metallic Coating Protection of Exposed AA2024-T3.* Journal of the Electrochemical Society, 2006. **153**(11): p. B486-B498.
60. Mizuno, D. and R. Kelly, *Galvanically Induced Intergranular Corrosion of AA5083-H131 Under Atmospheric Exposure Conditions: Part 1-Experimental Characterization.* Corrosion, 2013. **69**(6): p. 580-592.
61. Nazir, M.H. and Z. Khan, *Maximising the interfacial toughness of thin coatings and substrate through optimisation of defined parameters.* International Journal of Computational Methods and Experimental Measurements, 2015. **3**(4): p. 316-328.
62. Bajwa, R.S., et al., *Effect of bath ionic strength on adhesion and tribological properties of pure nickel and Ni-based nanocomposite coatings.* Journal of adhesion science and Technology, 2016. **30**(6): p. 653-665.
63. Tong, L. and R.G. Reddy, *Synthesis of titanium carbide nano-powders by thermal plasma.* Scripta materialia, 2005. **52**(12): p. 1253-1258.
64. Latif, J., et al., *Condition monitoring and predictive modelling of coating delamination applied to remote stationary and mobile assets.* Structural Health Monitoring, 2019. **18**(4): p. 1056-1073.
65. Lenert, A. and E.N. Wang, *Optimization of nanofluid volumetric receivers for solar thermal energy conversion.* Solar Energy, 2012. **86**(1): p. 253-265.
66. Yang, H., L. Lu, and W. Zhou, *A novel optimization sizing model for hybrid solar-wind power generation system.* Solar energy, 2007. **81**(1): p. 76-84.
67. Bernal-Agustín, J.L. and R. Dufo-López, *Simulation and optimization of stand-alone hybrid renewable energy systems.* Renewable and Sustainable Energy Reviews, 2009. **13**(8): p. 2111-2118.
68. Pawar, V.R. and S. Sobhansarbandi, *Design optimization and heat transfer enhancement of energy storage based solar thermal collector.* Sustainable Energy Technologies and Assessments, 2021. **46**: p. 101260.
69. Paul, J., et al., *A comprehensive review on thermophysical properties and solar thermal applications of organic nano composite phase change materials.* Journal of Energy Storage, 2022. **45**: p. 103415.

Declaration of Competing Interest

The authors declare the following financial interests/personal relationships which may be considered as potential competing interests. Dr Hammad Nazir reports a relationship with University of South Wales that includes: employment. If there are other authors, they declare that they have no known competing financial interests or personal relationships that could have appeared to influence the work reported in this paper.